

Weak radiative corrections to dijet production at hadron colliders

STEFAN DITTMAYER, ALEXANDER HUSS
AND CHRISTIAN SPECKNER

*Albert-Ludwigs-Universität Freiburg, Physikalisches Institut,
D-79104 Freiburg, Germany*

Abstract:

We present the calculation of the most important electroweak corrections to dijet production at the LHC and the Tevatron, comprising tree-level effects of $\mathcal{O}(\alpha_s\alpha, \alpha^2)$ and weak loop corrections of $\mathcal{O}(\alpha_s^2\alpha)$. Although negligible for integrated cross sections, these corrections can reach 10–20% in the TeV range for transverse jet momenta k_T . Our detailed discussion of numerical results comprises distributions in the dijet invariant mass and in the transverse momenta of the leading and subleading jets. We find that the weak loop corrections amount to about -12% and -10% for leading jets with $k_T \sim 3$ TeV at the 14 TeV LHC and $k_T \sim 800$ GeV at the Tevatron, respectively. The electroweak tree-level contributions are of the same generic size and typically positive at the LHC and negative at the Tevatron at high energy scales. Generally the corrections to the dijet invariant mass distributions are smaller by at least a factor of two as compared to the corresponding reach in the k_T distributions, because unlike the k_T spectra the invariant-mass distributions are not dominated by the Sudakov regime at high energy scales.

October 2012

1 Introduction

The unprecedented energy regime that is accessible at the LHC allows for the investigation of the laws of physics at the smallest distances. The inclusive production of two jets (dijets) at the LHC, $pp \rightarrow jj + X$, allows for a detailed study of QCD at TeV energies. Furthermore, several extensions of the Standard Model predict new heavy particles which might be visible via dijet signatures in the detector [1]. Some examples are excited states of composite quarks q^* , string resonances, new heavy gauge bosons W', Z' , etc. Inclusive jet and dijet production has been analyzed by the ATLAS [2] and CMS [3] collaborations at a centre-of-mass (CM) energy of 7 TeV giving sensitivity to dijet invariant masses of up to 5 TeV and jet transverse momenta of up to 2 TeV at the LHC. The Tevatron experiments CDF [4] and D0 [5] have investigated jet production up to transverse momenta of several hundreds of GeV. At the current level of experimental and theoretical accuracy, the SM is able to describe data quite well. At the LHC design CM energy of 14 TeV, the energy reach will even go deeper into the TeV range, so that theoretical predictions especially have to carefully include radiative corrections that are sensitive to high scales.

The results for the production of two jets at leading-order (LO) accuracy in QCD had been available [6] long before higher-order corrections were established. Later, in the 1990s, the differential cross sections to inclusive single-jet and two-jet production were discussed at next-to-leading order (NLO) accuracy in QCD [7–9]. Currently, enormous effort is put into the calculation of the NNLO QCD corrections to dijet production (see e.g. Refs. [10–16] and references therein). The purely weak corrections of $\mathcal{O}(\alpha_s^2\alpha)$ have been calculated for the single-jet-inclusive cross section in Ref. [17], and preliminary results of the weak corrections to the dijet production were published in Ref. [18]. The two results, however, do not seem compatible with each other. Electroweak corrections also were calculated for the related process of bottom-jet production [19].

In spite of their suppression by the small value of the coupling constant α , the electroweak (EW) corrections can become large in the high-energy domain [20–27]. This is due to the appearance of Sudakov-type and other high-energy logarithms that result from the virtual exchange of soft or collinear massive weak gauge bosons. The leading term is given by $\alpha_w \ln^2(Q^2/M_W^2)$, where Q denotes a typical energy scale of the hard-scattering reaction, M_W is the W-boson mass, and $\alpha_w = \alpha/s_w^2 = e^2/(4\pi s_w^2)$ is derived from the $SU(2)$ gauge coupling e/s_w with s_w denoting the sine of the weak mixing angle θ_w . In the case of massless gauge bosons, e.g. in QED or QCD, these logarithms are connected to the well-known infrared divergences and are cancelled against the corresponding real-emission corrections. For the massive gauge bosons W and Z, no such singularities occur, since their masses provide a physical cut-off and the additional radiation of real W or Z bosons can be experimentally reconstructed to a large extent, so that W/Z bremsstrahlung corresponds to a different class of processes. Thus, at high scales $|Q^2| \gg M_W^2$, which are accessible at the LHC and the Tevatron, the above Sudakov-type logarithms can produce large negative corrections, as only some fractions are compensated by unresolved W/Z emission [28]. It turns out that large compensations can occur between different electroweak logarithms [29, 30], so that a full fixed-order calculation desirable.

As it will be discussed in more detail below, a gauge-invariant classification of the EW corrections into photonic and purely weak corrections is feasible for our process. Guided

by the logarithmic enhancements, we restrict ourselves to the calculation of the purely weak corrections in this paper. The calculation can be complemented by the photonic corrections at a later time to produce results for the full EW corrections at the order $\alpha_s^2\alpha$.

The paper is organized as follows: In Section 2 we set up our conventions (Sect. 2.1) and discuss our strategy for the calculation of the NLO corrections (Sect. 2.2). The numerical results are presented in Section 3, which comprises integrated cross sections as well as differential distributions and the comparison to other work. Section 4 contains our conclusions.

2 Dijet production in hadronic collisions

2.1 Conventions and calculational setup

We consider the hadronic process

$$A(p_A) + B(p_B) \rightarrow j(k_1) + j(k_2) + X, \quad (2.1)$$

where the assignment of the four-momenta to the respective particles is indicated in parentheses. We further assume that the momenta k_1 and k_2 are sorted in a descending order with respect to their transverse momenta, i.e. $k_{T,1} \geq k_{T,2}$, referring to the associated jets as the leading and subleading jet, respectively. The hadronic cross section is given by the incoherent sum over the different partonic subprocesses that contribute to the final state under consideration, convoluted with the respective parton distribution functions (PDFs),

$$\sigma_{AB}(p_A, p_B) = \sum_{a,b} \int_0^1 dx_a \int_0^1 dx_b f_{a|A}(x_a, \mu_F^2) f_{b|B}(x_b, \mu_F^2) \hat{\sigma}_{ab}(p_a, p_b). \quad (2.2)$$

The PDF $f_{a|A}(x_a, \mu_F^2)$ plays the role of a generalized number density to find a parton a carrying the momentum fraction x_a of the parent hadron A with $p_a = x_a p_A$ denoting the four-momentum of the incoming parton to the hard scattering. We work in the QCD-improved parton model using the five-flavour scheme with $N_f = 5$ massless quarks $q = u, d, c, s, b$. The partonic subprocesses that contribute to the above scattering reaction at NLO can be generically written as

$$a(p_a) + b(p_b) \rightarrow c(k_c) + d(k_d) (+e(k_e)), \quad (2.3)$$

where $a, b, c, d, e \in \{g, u, d, c, s, b\}$ if only weak corrections are considered. For photonic corrections also the photon has to be included as a possible external particle state. The additional emission of parton e appears in the real NLO correction to this process. The momenta k_1 and k_2 in Eq. (2.1) emerge from the recombination procedure of the jet algorithm. At LO, however, we simply have $k_1 = k_c$, $k_2 = k_d$, with $k_{T,1} = k_{T,2}$. Owing to the mass degeneracy ($m_q = 0$) of the external quarks and the unitarity of the CKM matrix, the effect of the non-diagonal CKM structure vanishes in most contributions after taking the flavour sums. The only exception is the case of a W-boson exchange in the s -channel, where the different weights from the PDFs spoils the cancellation. However, this dependence turns out to be negligible and we set the CKM matrix to unity in our calculation.

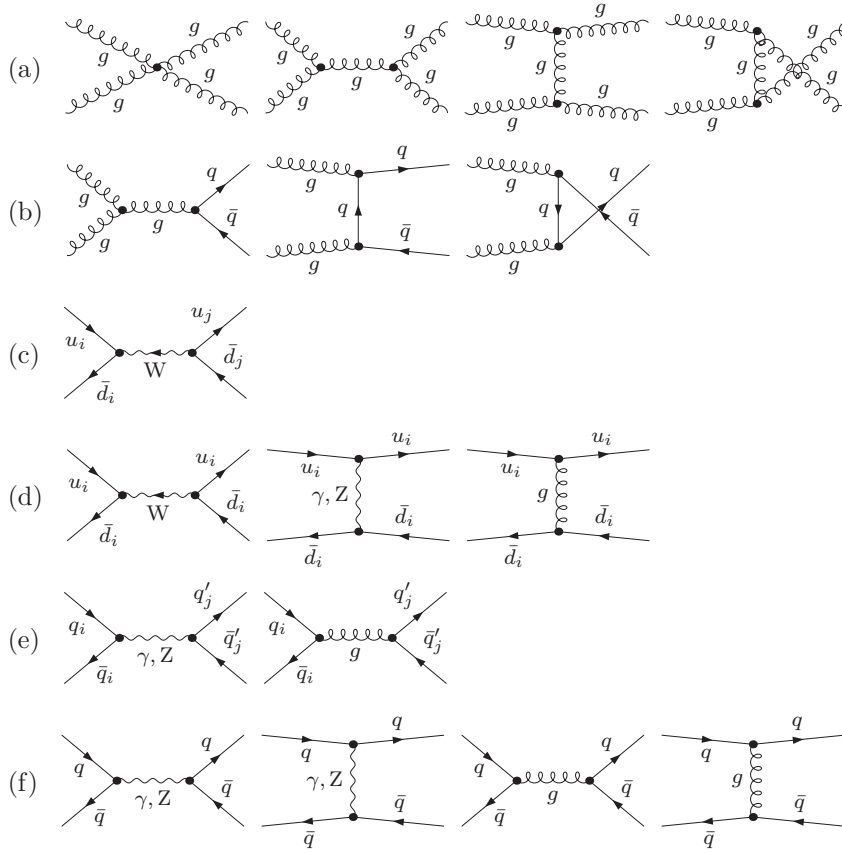


Figure 1: Tree-level Feynman graphs (a–f) to the processes (2.4a–f), respectively.

The partonic subprocesses can be classified as follows:

$$g + g \rightarrow g + g, \quad (2.4a)$$

$$g + g \rightarrow q + \bar{q}, \quad (2.4b)$$

$$u_i + \bar{d}_i \rightarrow u_j + \bar{d}_j, \quad (i \neq j), \quad (2.4c)$$

$$u_i + \bar{d}_i \rightarrow u_i + \bar{d}_i, \quad (2.4d)$$

$$q_i + \bar{q}_i \rightarrow q'_j + \bar{q}'_j, \quad (i \neq j), \quad (2.4e)$$

$$q + \bar{q} \rightarrow q + \bar{q}, \quad (2.4f)$$

where i, j denote the generation indices. We note that the processes listed in Eq. (2.4) are merely representatives of a class that also include the reactions that are related by crossing symmetry. First, we categorize the processes according to the number of gluons and quarks that appear as external particles into the four-gluon (a), the two-gluon–two-quark (b), and the four-quark (c–f) processes. The four-quark processes can be subdivided into processes that involve a W-boson exchange diagram (c,d) and those that only contain neutral-boson exchange diagrams (e,f). A further distinction is made by distinguishing processes that involve both s -channel and t -channel diagrams (c,e), and those that only include either one (d,f). The LO Feynman graphs to the above process classes are shown in Fig. 1. Furthermore, we can exploit the symmetry of the matrix element with respect to the interchange of the generation index of the first two quark generations. This reduces the

number of independent amplitudes that need to be evaluated and speeds up the numerical evaluation.

The electroweak coupling constant is derived from the Fermi constant in the G_μ scheme via the following relation

$$\alpha_{G_\mu} = \frac{\sqrt{2}}{\pi} G_\mu M_W^2 \left(1 - \frac{M_W^2}{M_Z^2} \right). \quad (2.5)$$

This input-parameter scheme avoids large logarithms of the light fermion masses generated by the running of the coupling constant $\alpha(Q)$ from the Thomson limit ($Q = 0$) to the electroweak scale ($Q \sim M_W$) and furthermore absorbs universal corrections induced by the ρ parameter (see e.g. Ref. [31]).

In order to describe the resonances of the intermediate vector bosons Z and W , we employ the complex-mass scheme [32, 33], which fully respects gauge invariance. In this approach the square of the gauge-boson mass is defined as the position of the pole in the complex k^2 plane of the respective propagator with momentum k . The consistent replacement of the (squared) gauge-boson masses by complex values,

$$M_V^2 \rightarrow \mu_V^2 = M_V^2 - iM_V\Gamma_V, \quad V = W, Z, \quad (2.6)$$

induces the adaption of all real quantities. In particular, this results in a complex weak-mixing angle θ_w :

$$\cos^2 \theta_w \equiv c_w^2 = \frac{\mu_W^2}{\mu_Z^2}, \quad \sin^2 \theta_w \equiv s_w^2 = 1 - c_w^2. \quad (2.7)$$

In order to ensure the correctness of the presented results two independent calculations have been performed, resulting in two separate implementations for the numerical evaluation. Both calculations employ the Feynman-diagrammatic approach in the 't Hooft–Feynman gauge for the loops and the Catani–Seymour dipole subtraction approach [34, 35] to isolate and cancel infrared (IR) divergences. The results of the two calculations are in mutual agreement.

In the first calculation all tree-level amplitudes are calculated and implemented by hand using the Weyl–van-der-Waerden spinor formalism as worked out in Ref. [36]. The virtual corrections are calculated using the MATHEMATICA Packages FEYNARTS 3.6 [37] and FORMCALC 6.2 [38]. The one-loop integrals are evaluated using a modified version of the LOOPTOOLS 2.4 [38] library, which was supplemented by the loop integrals with dimensionally regularized IR divergences that were not included in version 2.4. Additionally, an interface is implemented between LOOPTOOLS and the COLLIER library, which is based on the results of Refs. [39, 40] for tensor and scalar one-loop integrals, respectively. This allows to utilize the unmodified code generated by FORMCALC, while resorting to COLLIER for the evaluation of the loop integrals. The results of the two approaches are in perfect mutual agreement. The numerical integration is performed using the adaptive Monte Carlo algorithm VEGAS [41], where a specific phase-space parametrization is chosen.

The second calculation uses FEYNARTS 1.0 [42] for generating the tree-level and one-loop diagrams and in-house MATHEMATICA routines to obtain an analytic result which then is exported as FORTRAN source code. The loop integrals are evaluated using the

COLLIER loop library. The finite Catani–Seymour dipole subtraction terms and real emission matrix elements are built around amplitudes generated with the O’MEGA [43] matrix-element generator. Adaptive single-channel Monte Carlo integration is implemented using the VAMP [44] library. Contrary to the first calculation, the second calculation does not implement subprocesses involving external bottom quarks which only amount to $\approx 3\%$ of the LO cross section and thus can be safely neglected at order $\alpha_s^2\alpha_s$. For all other subprocesses, both calculations are in excellent agreement for both the integrated and differential cross sections.

2.2 Structure of the NLO calculation

The calculation of the LO cross section is based on the full SM, i.e. all vector bosons, including the photon γ , are included. The Born diagrams for each process class defined in the previous section are shown in Fig. 1.

At NLO we classify the corrections into photonic and purely weak corrections. This is possible, because each diagram in the full NLO correction, defined by the order $\alpha_s^2\alpha$, contains exactly one electroweak gauge boson due to the single power in α . We can therefore uniquely assign each NLO contribution to either a photonic or a purely weak correction. The photonic corrections would constitute the $\mathcal{O}(\alpha_s^2\alpha)$ corrections in a hypothetical gauge theory with the group $SU(3)_C \times U(1)_{\text{QED}}$. Therefore, they form a gauge-invariant subset and consequently so do the remaining purely weak corrections. In the following, we will use the notation $\mathcal{O}(\alpha_s^2\alpha_w)$ to refer to the purely weak contributions.

This gauge-invariant classification of the corrections allows us to tackle each class successively. In this work we present the calculation of the $\mathcal{O}(\alpha_s^2\alpha_w)$ corrections, as motivated in the introduction. The inclusion of the photonic corrections in order to obtain the full EW corrections at the order $\alpha_s^2\alpha$ is left to the future.

It is known [28, 45] that partial cancellations can occur between the virtual weak corrections and the real emission of massive gauge bosons. However, to which extent this compensation takes place strongly depends on the experimental setup to reconstruct W and Z bosons. Considering that the weak-boson emission is a tree-level process which can be easily simulated with fully LO automatic tools, they are not further considered here.

2.2.1 Virtual corrections

The virtual corrections consist of the one-loop diagrams and the corresponding counterterms. Because we are restricting our NLO calculation to the order $\mathcal{O}(\alpha_s^2\alpha_w)$, only the interference terms shown in Fig. 2 are relevant. The generic diagram for the virtual corrections to the process class (2.4b) is shown in Fig. 2(a). The corrections constitute the purely weak $\mathcal{O}(\alpha_w)$ correction to the LO $\mathcal{O}(\alpha_s^2)$ cross section; some representative diagrams are depicted in Fig. 2(a’). In case of the process classes (2.4d–f) with four external quarks, however, we have LO amplitudes of the order α_w and α_s . This leads to the two types of virtual corrections shown in Figs. 2(b,c). Here, we can identify genuine QCD corrections, such as the contributions shown in Fig. 2(c’) and the first vertex correction in Fig. 2(b’), and weak corrections, such as the second vertex correction in Fig. 2(b’). However, there are also contributions such as the box diagram in Fig. 2(b’) that cannot be assigned uniquely to QCD nor to weak corrections. This indicates that the separation

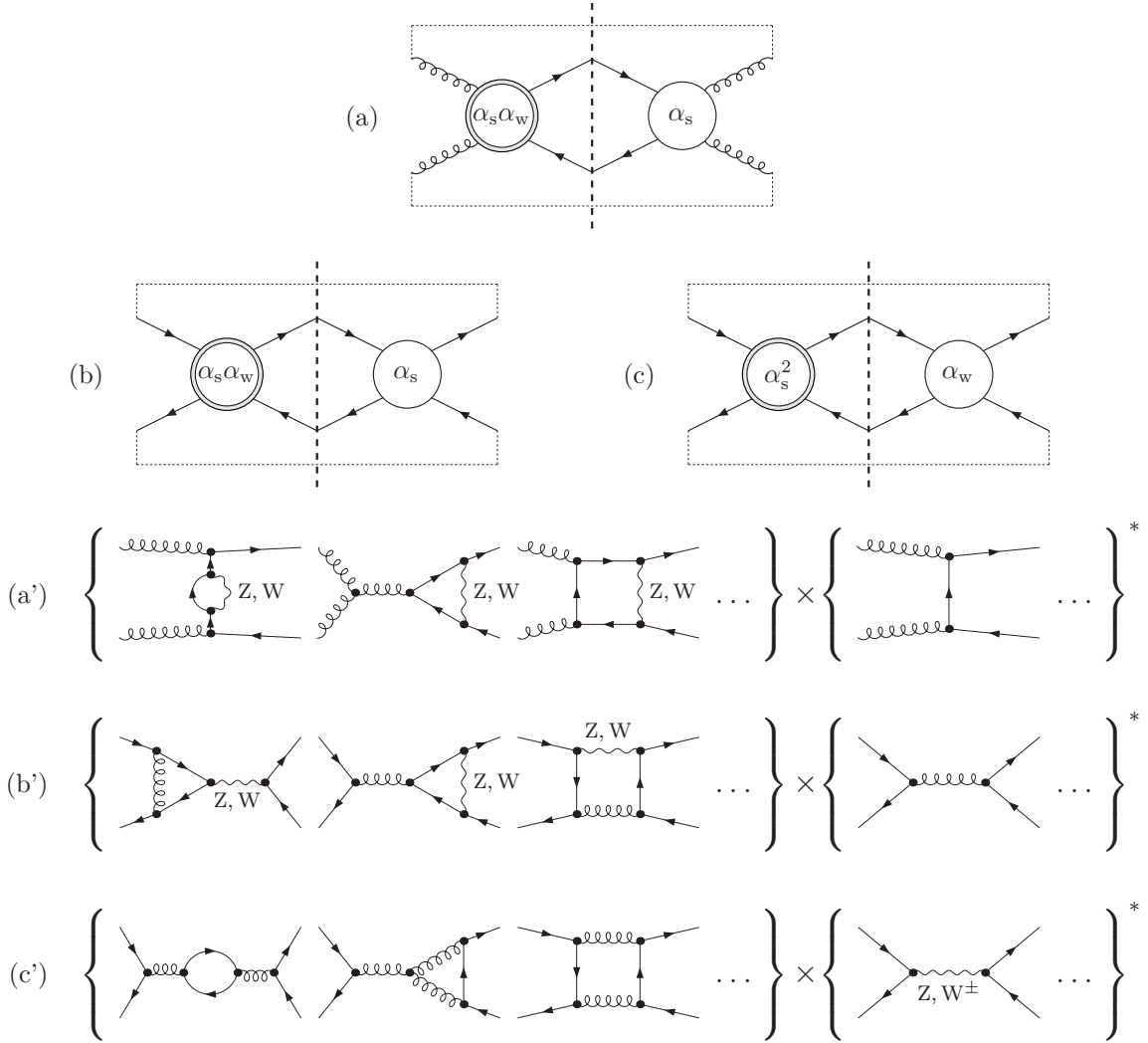


Figure 2: The virtual corrections of $\mathcal{O}(\alpha_s^2 \alpha_w)$ illustrated in terms of interference diagrams of generic Feynman graphs (a-c) and a set of sample diagrams below (a'-c'). The white circles and the double-circles in the interference diagrams represent tree-level and one-loop subgraphs, respectively.

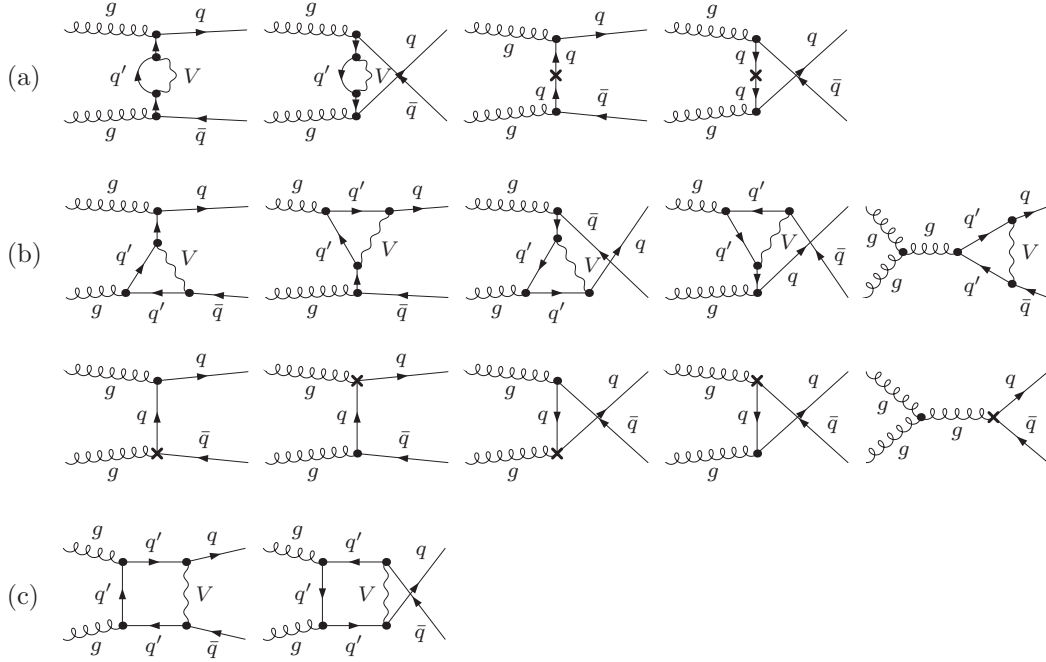


Figure 3: One-loop and counterterm diagrams for the process class (2.4b) grouped into the self-energy (a), vertex (b), and box (c) corrections. All counterterms are restricted to the order $\mathcal{O}(\alpha_w)$. V denotes the vector bosons W and Z , and q' the weak-isospin partner of q for $V = W$ and $q' = q$ for $V = Z$.

of the “QCD corrections” from the “weak corrections” is not properly defined and instead, one must treat them together as a whole, defined by the order in perturbation theory. The contributions we referred to by the “QCD corrections” above contain infrared divergences and, therefore, the real emission of an additional gluon must be considered, which will be discussed in the next section. A more complete set of one-loop and counterterm diagrams associated with the schematic illustrations in Figs. 2(a), 2(b), and 2(c) can be found in Figs. 3, 4, and 5, respectively.¹

Ultraviolet (UV) divergences are regularized dimensionally. For the IR singularities also dimensional regularization is used, but our second calculation optionally employs infinitesimal masses as regulators. It has been shown in the appendix of Ref. [46] that rational terms of IR origin cancel in any unrenormalized scattering amplitude, so that they need not be further considered in the calculation of the one-loop amplitudes. The only remaining source of rational terms of IR origin involve the wave-function renormalization constants, which were calculated separately and are given below.

The external fields are renormalized in the on-shell scheme and hence, all self-energy corrections to the external (on-shell) legs vanish and can be omitted already at the level of diagram generation. The renormalization of the strong coupling constant is done using the $\overline{\text{MS}}$ scheme for the $N_f = 5$ light quarks and by subtracting the contribution of the

¹In the case with external bottom quarks there exist additional diagrams in Fig. 3 and Fig. 4(b) due to the non-vanishing mass of the weak-isospin partner t , where in place of W^\pm a charged would-be Goldstone boson ϕ^\pm is exchanged.

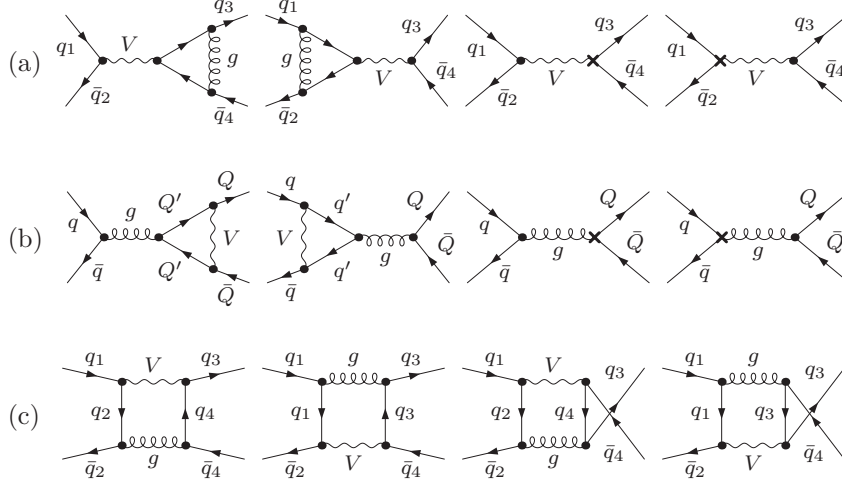


Figure 4: One-loop and counterterm diagrams for the processes (2.4)(d-f) of $\mathcal{O}(\alpha_s\alpha_w)$ grouped into vertex (a,b) and box (c) corrections. The triangle insertions are further subdivided into QCD (a) and weak (b) corrections, and consequently the associated counterterms are restricted to the order $\mathcal{O}(\alpha_s)$ and $\mathcal{O}(\alpha_w)$, respectively. V denotes the vector bosons W and Z .

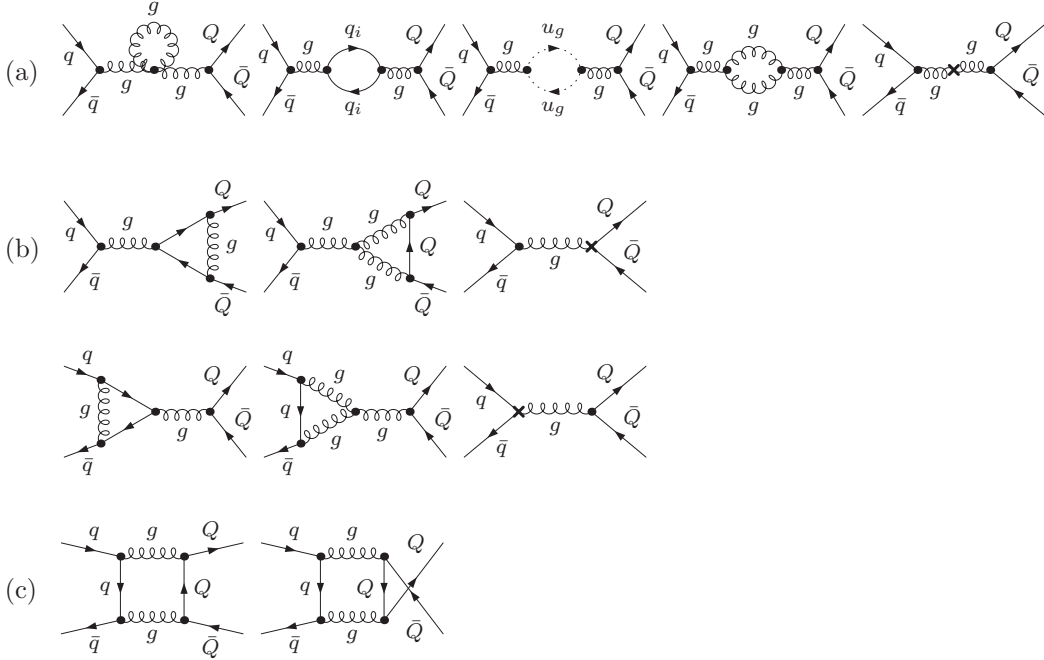


Figure 5: One-loop and counterterm diagrams for the processes (2.4)(d-f) of $\mathcal{O}(\alpha_s^2)$ grouped into self-energy (a), vertex (b), and box (c) corrections. All counterterms are restricted to the order $\mathcal{O}(\alpha_s)$.

heavy top-quark loop in the gluon self-energy at zero momentum transfer. Therefore, the running of the strong coupling constant is driven by the five light quark flavours only.

Similar to the loop diagrams, the renormalization constants need to be evaluated at different orders, where the ones of $\mathcal{O}(\alpha_s)$ are

$$\delta Z_{g_s}|_{\mathcal{O}(\alpha_s)} = -\frac{\alpha_s}{4\pi} \left[\left(\frac{11}{2} - \frac{N_f}{3} \right) \left(\Delta_{\text{UV}} + \ln \left(\frac{\mu^2}{\mu_R^2} \right) \right) - \frac{1}{3} B_0(0, m_t, m_t) \right], \quad (2.8)$$

$$\delta Z_G|_{\mathcal{O}(\alpha_s)} = \frac{\alpha_s}{2\pi} \left[\left(\frac{5}{2} - \frac{N_f}{3} \right) B_0(0, 0, 0) - \frac{1}{3} B_0(0, m_t, m_t) \right], \quad (2.9)$$

$$\delta Z_q|_{\mathcal{O}(\alpha_s)} = -\frac{\alpha_s}{3\pi} B_0(0, 0, 0), \quad (2.10)$$

and the ones of $\mathcal{O}(\alpha_w)$ are

$$\delta Z_q^L|_{\mathcal{O}(\alpha_w)} = \frac{\alpha}{4\pi} \left[(g_q^-)^2 (1 + 2B_1(0, 0, \mu_Z)) + \frac{1}{2s_w^2} (1 + 2B_1(0, 0, \mu_W)) \right], \quad (2.11)$$

$$\delta Z_q^R|_{\mathcal{O}(\alpha_w)} = \frac{\alpha}{4\pi} (g_q^+)^2 (1 + 2B_1(0, 0, \mu_Z)), \quad (2.12)$$

where our notation for the 2-point functions $B_{0,1}$ follows Ref. [39], μ is the arbitrary reference mass of dimensional regularization, μ_R the renormalization scale, and

$$\Delta_{\text{UV}} = \frac{2}{4-D} - \gamma_E + \ln(4\pi) \quad (2.13)$$

denotes the standard one-loop UV divergence in D dimensions. Here $\delta Z_q^{\text{R/L}}$ and δZ_G are the field-renormalization constants of the right/left-handed quark fields and of the gluon field, respectively, and δZ_{g_s} connects the bare ($g_{s,0}$) and the renormalized (g_s) strong coupling constant, $g_{s,0} = (1 + \delta Z_{g_s})g_s$. The couplings g_q^\pm are defined via the 3rd component of weak-isospin, $I_{w,q}^3$, and the electric charge Q_q of the quark q ,

$$g_q^- = \frac{I_{w,q}^3 - s_w^2 Q_q}{s_w c_w}, \quad g_q^+ = -\frac{s_w}{c_w} Q_q, \quad (I_{w,q}^3, Q_q) = \begin{cases} (+1/2, +2/3), & q = u_i, \\ (-1/2, -1/3), & q = d_i. \end{cases} \quad (2.14)$$

At this point some comments on the use of complex masses and couplings, as dictated by the complex-mass scheme [32, 33], are appropriate. This scheme, which was primarily introduced to achieve a consistent, gauge-invariant description of gauge-boson resonances at LO and NLO, does not only comprise the consistent use of complex parameters in amplitudes, but also complex generalizations of the renormalization constants for the complex masses and couplings as compared to on-shell renormalization schemes for real masses (see e.g. Ref. [47]). Note, however, that the order $\mathcal{O}(\alpha_s^2 \alpha)$ of the corrections considered in this calculation does not involve weak corrections to gauge-boson propagators and weak couplings, so that the complex generalization of the relevant renormalization constants given in Eqs. (2.8)–(2.12) just concerns the insertion of complex masses and weak couplings.

2.2.2 Real corrections

The real corrections receive contributions from the partonic processes that are illustrated in terms of interference diagrams in Fig. 6. The contribution shown in Fig. 6(a)

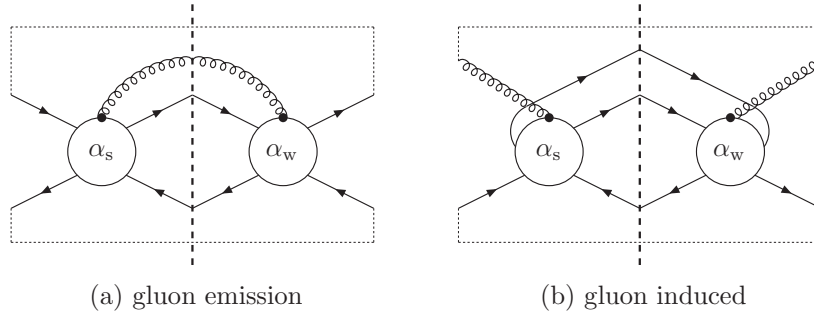


Figure 6: The real corrections at $\mathcal{O}(\alpha_s^2\alpha_w)$ illustrated in terms of interference diagrams of generic Feynman graphs. The circles represent tree-level subgraphs.

corresponds to the additional emission of a gluon from the processes (2.4d–f), properly taking into account only the interference terms that contribute at the order $\mathcal{O}(\alpha_s^2\alpha_w)$. The gluon-induced corrections in Fig. 6(b) are obtained from the preceding by crossing the gluon into the initial state.

The real-emission cross section contains infrared divergences in the phase-space integration which have their origin in the regions where a final-state parton becomes soft or collinear to another parton. The soft and the final-state collinear singularities cancel against the corresponding singularities in the virtual corrections for sufficiently inclusive observables by virtue of the Kinoshita–Lee–Nauenberg theorem [48, 49]. The remaining initial-state collinear singularities are process independent and absorbed into the NLO PDFs by QCD factorization, which is technically accomplished by subtracting a so-called collinear counterterm ($d\sigma^C$) from the NLO cross section. The subtraction formalism reshuffles the IR singularities by constructing a subtraction term ($d\sigma^A$) to the real correction ($d\sigma^R$) which mimics its singular behaviour to render their difference integrable in four dimensions. The subtraction term can be integrated analytically in $D = 4 - 2\epsilon$ dimensions over the singular one-particle subspace, generating $1/\epsilon$ and $1/\epsilon^2$ poles that cancel against the corresponding poles in the virtual corrections ($d\sigma^V$) and the collinear counterterm.

To this end, we employ the Catani–Seymour dipole subtraction formalism [34], which constructs the subtraction term in terms of so-called dipoles, which are built from the LO amplitudes (σ^B) and dipole operators (dV_{dipole}) which in general contain colour and helicity correlations. The NLO contribution to the hard-scattering cross section from Eq. (2.2) can be schematically written as,

$$\begin{aligned}
\sigma^{\text{NLO}} &= \int_3 d\sigma^R + \int_2 d\sigma^V + \int_2 d\sigma^C \\
&= \int_3 \left[(d\sigma^R)_{\epsilon=0} - (d\sigma^A)_{\epsilon=0} \right] + \int_2 \left[d\sigma^V + d\sigma^C + \int_1 d\sigma^A \right]_{\epsilon=0} \\
&= \int_3 \left[(d\sigma^R)_{\epsilon=0} - \left(\sum_{\text{dipoles}} d\sigma^B \otimes dV_{\text{dipole}} \right)_{\epsilon=0} \right] \\
&\quad + \int_2 \left[d\sigma^V + d\sigma^B \otimes \mathbf{I}(\epsilon) \right]_{\epsilon=0} + \int_0^1 dx \int_2 d\sigma^B \otimes (\mathbf{K}(x) + \mathbf{P}(x, \mu_F^2)), \quad (2.15)
\end{aligned}$$

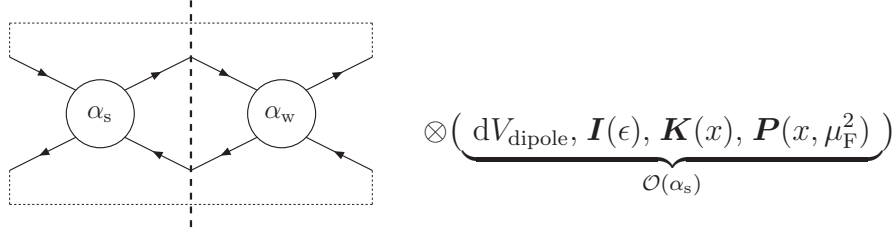


Figure 7: The building blocks for the subtraction terms at $\mathcal{O}(\alpha_s^2\alpha_w)$ illustrated in terms of interference diagrams of generic Feynman graphs. The circles represent tree-level subgraphs. The symbol \otimes denotes possible colour and helicity correlations between the dipole operators and the LO amplitudes.

where \int_m denotes the integration over the m -particle phase space, \otimes encodes the possible colour and helicity correlations between $d\sigma^B$ and the dipole operators, and the integration over x corresponds to a convolution over the momentum fraction of the incoming partons. The insertion operators $\mathbf{I}(\epsilon)$, $\mathbf{K}(x)$, and $\mathbf{P}(x, \mu_F^2)$ emerge from the collinear counterterm and the integration of the subtraction term over the singular one-particle subspace. More details and the explicit expressions for $\mathbf{I}(\epsilon)$, $\mathbf{K}(x)$, and $\mathbf{P}(x, \mu_F^2)$ can be found in Ref. [34].

The dipole operators introduced above are all of $\mathcal{O}(\alpha_s)$, which in turn forces us to restrict the calculation of the colour-correlated LO amplitudes to the interference terms of $\mathcal{O}(\alpha_s\alpha_w)$. This is schematically illustrated in Fig. 7.

For the second calculation which used both dimensional and mass regularization for the IR divergences, the generalization of the above formalism for massive partons [35] is used for the latter scheme.

3 Numerical results

3.1 Input parameters and setup

For the numerical evaluation we use the input parameters of Ref. [50],

$$\begin{aligned}
 G_\mu &= 1.16637 \times 10^{-5} \text{ GeV}^{-2}, & \alpha_s(M_Z) &= 0.129783, \\
 M_W^{\text{OS}} &= 80.398 \text{ GeV}, & M_Z^{\text{OS}} &= 91.1876 \text{ GeV}, \\
 \Gamma_W^{\text{OS}} &= 2.141 \text{ GeV}, & \Gamma_Z^{\text{OS}} &= 2.4952 \text{ GeV}, \\
 m_t &= 172.5 \text{ GeV}. & &
 \end{aligned} \tag{3.1}$$

Note that there is no Higgs-boson mass dependence in the predictions for dijet production at the considered order. The complex-mass scheme for the W and Z bosons corresponds to a fixed-width description of the resonance and requires a conversion of the on-shell gauge-boson masses to the pole masses M_V^{OS} as follows [51],

$$M_V = \frac{M_V^{\text{OS}}}{c_V}, \quad \Gamma_V = \frac{\Gamma_V^{\text{OS}}}{c_V}, \quad c_V = \sqrt{1 + \left(\frac{\Gamma_V^{\text{OS}}}{M_V^{\text{OS}}}\right)^2}, \tag{3.2}$$

giving

$$\begin{aligned}
M_W &= 80.3695 \dots \text{GeV}, & M_Z &= 91.1535 \dots \text{GeV}, \\
\Gamma_W &= 2.1402 \dots \text{GeV}, & \Gamma_Z &= 2.4943 \dots \text{GeV}.
\end{aligned}
\tag{3.3}$$

For the PDFs we use the CTEQ6L1 [52] set, which dictates the value of $\alpha_s(M_Z)$ in Eq. (3.1). A consistent QCD calculation, of course, requires the use of LO, NLO, or NNLO PDFs for the calculation of the respective cross-section prediction. Our aim here is, however, to provide a relative correction factor for weak effects that is to be applied to state-of-the-art QCD predictions. This factorization procedure is better motivated than just adding QCD and electroweak corrections because of the factorization of IR-sensitive corrections. The weak correction factor has to be derived from a single PDF set, but is rather insensitive to PDFs.² The renormalization scale is set equal to the factorization scale, chosen as the transverse momentum of the leading jet

$$\mu_R = \mu_F \equiv \mu = k_{T,1}. \tag{3.4}$$

3.2 Phase-space cuts and event selection

The definition of an IR-safe jet observable requires the recombination of soft and/or collinear partons in the final state, as well as constraining the phase space by imposing cuts. The jets emerge from the final-state partons via the anti- k_T algorithm [53], where we have set the angular separation parameter to $R = 0.6$. Recombination is performed using four-momentum summation.

We require the jets to have transverse momenta $k_{T,i}$ larger than $k_{T,\text{jet}}^{\text{cut}}$ and demand them to be central by restricting their rapidities y_i to the range $|y_i| < y_{\text{jet}}^{\text{cut}}$ with the values

$$y_{\text{jet}}^{\text{cut}} = 2.5, \quad k_{T,\text{jet}}^{\text{cut}} = 25 \text{ GeV}. \tag{3.5}$$

3.3 Results

In the following, we present the numerical results for dijet production at the LHC, i.e. for a pp initial state, at the centre-of-mass (CM) energies of $\sqrt{s} = 7 \text{ TeV}$, 8 TeV , and 14 TeV , and at the Tevatron, i.e. for $p\bar{p}$ collisions at the CM energy of $\sqrt{s} = 1.96 \text{ TeV}$.

We denote the full LO cross section through $\mathcal{O}(\alpha_s^2, \alpha_s\alpha, \alpha^2)$ by σ^0 and define the NLO corrections relative to the LO cross section via

$$\sigma^{\text{NLO}} = \sigma^0 \times (1 + \delta_{\text{weak}}^{\text{1-loop}}). \tag{3.6}$$

Furthermore, we denote the LO QCD cross section of $\mathcal{O}(\alpha_s^2)$ by σ_{QCD}^0 and introduce a correction factor for the left-over LO contributions of order $\alpha_s\alpha$ and α^2 ,

$$\sigma^0 = \sigma_{\text{QCD}}^0 \times (1 + \delta_{\text{EW}}^{\text{tree}}). \tag{3.7}$$

²The consistent use of LO PDFs is fully justified for the electroweak tree-level contributions and the weak loop corrections (containing the large weak Sudakov logarithms) to the QCD channels. The remaining part of the calculated correction actually has the character of a QCD correction, viz. the interference of QCD loops with weak LO diagrams and the corresponding real corrections, strictly requiring NLO PDFs. Recall, however, that the two different loop contributions cannot be separated, as explained in Sect. 2.2. Since the calculated corrections are generally rather moderate, our procedure is certainly acceptable within the remaining uncertainty of the aimed combination of QCD and weak corrections.

pp \rightarrow $jj + X$ at $\sqrt{s} = 7$ TeV

M_{12}/GeV	50 – ∞	100 – ∞	200 – ∞	500 – ∞	1000 – ∞	2000 – ∞	3000 – ∞
σ^0/nb	78600(2)	25496(1)	3879.2(3)	80.807(2)	2.49314(5)	$33.0487(9) \cdot 10^{-3}$	$890.83(1) \cdot 10^{-6}$
$\sigma_{\text{QCD}}^0/\text{nb}$	78561(2)	25490(1)	3878.07(10)	80.650(3)	2.4756(2)	$32.4826(8) \cdot 10^{-3}$	$870.69(2) \cdot 10^{-6}$
$\delta_{\text{weak}}^{1\text{-loop}}/\%$	-0.02	-0.03	-0.09	-0.39	-1.09	-2.48	-3.60
$\delta_{\text{EW}}^{\text{tree}}/\%$	0.05	0.01	0.04	0.20	0.70	1.75	2.31
$\sum \delta/\%$	0.02	-0.02	-0.05	-0.19	-0.38	-0.73	-1.29
$\sigma^{\text{NLO}}/\text{nb}$	78581(2)	25487(1)	3875.7(3)	80.493(2)	2.46627(6)	$32.244(1) \cdot 10^{-3}$	$859.48(4) \cdot 10^{-6}$

pp \rightarrow $jj + X$ at $\sqrt{s} = 8$ TeV

M_{12}/GeV	50 – ∞	100 – ∞	200 – ∞	500 – ∞	1000 – ∞	2000 – ∞	3000 – ∞
σ^0/nb	94683(2)	31201(1)	4868.2(3)	108.331(7)	3.65684(7)	$61.498(1) \cdot 10^{-3}$	$2.45475(6) \cdot 10^{-3}$
$\sigma_{\text{QCD}}^0/\text{nb}$	94638(2)	31197(2)	4867.1(1)	108.152(3)	3.6344(1)	$60.5237(9) \cdot 10^{-3}$	$2.40056(5) \cdot 10^{-3}$
$\delta_{\text{weak}}^{1\text{-loop}}/\%$	-0.02	-0.03	-0.08	-0.37	-1.05	-2.44	-3.62
$\delta_{\text{EW}}^{\text{tree}}/\%$	0.04	0.01	0.03	0.17	0.61	1.61	2.25
$\sum \delta/\%$	0.02	-0.02	-0.05	-0.20	-0.44	-0.83	-1.37
$\sigma^{\text{NLO}}/\text{nb}$	94661(2)	31191(1)	4864.1(3)	107.926(8)	3.61864(10)	$60.019(2) \cdot 10^{-3}$	$2.3678(1) \cdot 10^{-3}$

pp \rightarrow $jj + X$ at $\sqrt{s} = 14$ TeV

M_{12}/GeV	50 – ∞	100 – ∞	200 – ∞	500 – ∞	1000 – ∞	2000 – ∞	5000 – ∞
σ^0/nb	198483(4)	69335(3)	11858.2(8)	334.17(1)	14.9435(4)	$456.64(1) \cdot 10^{-3}$	$954.71(2) \cdot 10^{-6}$
$\sigma_{\text{QCD}}^0/\text{nb}$	198410(5)	69329(2)	11856.0(10)	333.849(8)	14.8938(3)	$452.12(2) \cdot 10^{-3}$	$930.90(3) \cdot 10^{-6}$
$\delta_{\text{weak}}^{1\text{-loop}}/\%$	-0.02	-0.03	-0.07	-0.31	-0.88	-2.20	-5.53
$\delta_{\text{EW}}^{\text{tree}}/\%$	0.03	0.01	0.02	0.10	0.34	1.00	2.56
$\sum \delta/\%$	0.01	-0.02	-0.05	-0.22	-0.55	-1.20	-2.98
$\sigma^{\text{NLO}}/\text{nb}$	198444(4)	69315(3)	11849.5(8)	333.12(1)	14.8117(4)	$446.69(2) \cdot 10^{-3}$	$903.19(7) \cdot 10^{-6}$

Table 1: Integrated dijet cross sections and respective corrections for various ranges of the dijet invariant mass M_{12} at the LHC with CM energies 7 TeV, 8 TeV, and 14 TeV.

For the NLO cross section this leads to

$$\begin{aligned}
\sigma^{\text{NLO}} &= \sigma_{\text{QCD}}^0 \times (1 + \delta_{\text{EW}}^{\text{tree}}) \times (1 + \delta_{\text{weak}}^{1\text{-loop}}) \\
&\simeq \sigma_{\text{QCD}}^0 \times (1 + \delta_{\text{EW}}^{\text{tree}} + \delta_{\text{weak}}^{1\text{-loop}}).
\end{aligned} \tag{3.8}$$

With respect to the LO QCD cross section, the total correction is given by the sum $\delta_{\text{weak}}^{1\text{-loop}} + \delta_{\text{EW}}^{\text{tree}}$. Owing to the rather moderate size of the corrections, the difference in defining the NLO corrections $\delta_{\text{weak}}^{1\text{-loop}}$ relative to σ^0 or σ_{QCD}^0 constitutes a higher-order effect which is negligible.

3.3.1 The dijet invariant mass at the LHC

The dijet invariant mass is defined as $M_{12} = \sqrt{(E_1 + E_2)^2 - (\mathbf{p}_1 + \mathbf{p}_2)^2}$, where $E_{1,2}$ and $\mathbf{p}_{1,2}$ denote the energies and the momenta of the leading and subleading jets, respect-

ively. In Table 1 we present the integrated LO cross sections σ^0 , σ_{QCD}^0 , the NLO cross section σ^{NLO} , and the relative correction factors $\delta_{\text{weak}}^{1\text{-loop}}$, $\delta_{\text{EW}}^{\text{tree}}$, $\sum \delta = \delta_{\text{EW}}^{\text{tree}} + \delta_{\text{weak}}^{1\text{-loop}}$ for different cuts on the dijet invariant mass M_{12} at the LHC. We note that the lowest cut value of $M_{12} > 50$ GeV is already covered by the standard setup via the cut on the transverse momenta of the jets, $k_{\text{T,jet}}^{\text{cut}} = 25$ GeV, and does not constitute a further restriction on the cross section.

The cross section is dominated by the region close to the cut, which is reflected by the rapid decrease of the integrated cross section with increasing values for the cut on M_{12} . Therefore, also the corrections are dominated by the region given by the lowest accepted M_{12} values.

Comparing the two cross sections σ^0 and σ_{QCD}^0 , we find that the LO cross section with minimal cuts is predominantly given by the QCD cross section and that the electroweak effects ($\delta_{\text{EW}}^{\text{tree}}$) typically stay below the per-cent level. However, we observe a steady increase in $\delta_{\text{EW}}^{\text{tree}}$ with higher M_{12} , which can be explained by the parton luminosities at the LHC: As can be seen from Fig. 8, the LO cross section is dominated at lower M_{12} by the gg - and gq -initiated processes, for which $\delta_{\text{EW}}^{\text{tree}}$ vanishes. At higher M_{12} , the qq -initiated processes with $\delta_{\text{EW}}^{\text{tree}} \neq 0$ become dominant, leading to the behaviour described above. The running of the strong coupling also acts in favour of increasing $\delta_{\text{EW}}^{\text{tree}}$ with higher cuts on M_{12} . Comparing the distributions in Fig. 8 for $\sqrt{s} = 7$ TeV and 14 TeV we observe a shift of the transition region from gg - to qq -domination from ~ 1.5 TeV to ~ 3 TeV, respectively. This trend is due to the fact that lower values of \sqrt{s} require larger partonic momentum fractions x for a fixed value of M_{12} , and the (valence) quark PDFs are enhanced over the gluon PDF for larger x . This also explains the \sqrt{s} dependence of the EW contribution $\delta_{\text{EW}}^{\text{tree}}$, which decreases with higher CM energies for the same cut on M_{12} .

The purely weak corrections are negative throughout and increase in magnitude from -0.02% to -3.6% in case of the $\sqrt{s} = 7$ TeV setup for a M_{12} cut of 50 GeV and 3 TeV, respectively. This behaviour partly originates from the corrections containing weak logarithms $\ln\left(\frac{M_{\text{W}}^2}{Q^2}\right)$, which become larger by effectively restricting the cross section to higher energy scales Q via increasing cuts on the invariant mass.

Compared to $\delta_{\text{EW}}^{\text{tree}}$, the relative weak corrections $\delta_{\text{weak}}^{1\text{-loop}}$ show a far weaker dependence on the CM energy. The corrections $\delta_{\text{EW}}^{\text{tree}}$ and $\delta_{\text{weak}}^{1\text{-loop}}$ are similar in magnitude, but of opposite sign, leading to large cancellations in the sum.

Note that the weak loop corrections $\delta_{\text{weak}}^{1\text{-loop}}$ in the TeV range are small in comparison to the typical size of the EW Sudakov factor $\frac{\alpha_{\text{W}}}{\pi} \ln^2\left(\frac{M_{\text{W}}^2}{Q^2}\right)$, which amounts to tens of per cent. This is due to the fact that also for large invariant mass M_{12} the cross section is not dominated by the Sudakov regime which requires that the absolute values of both partonic Mandelstam variables $\hat{s} = (p_a + p_b)^2$ and $\hat{t} = (p_a - k_c)^2$ are much larger than M_{W}^2 . Instead, the cross section here is dominated by the Regge (forward) region where \hat{s} is large, but $|\hat{t}|$ remains small.

This feature is also evident in the dijet invariant-mass distributions shown in Fig. 9. The relative corrections given in Table 1 are almost identical to the corrections in Fig. 9 at the respective cut value of M_{12} , since the corrections are dominated by the region close to the cut.

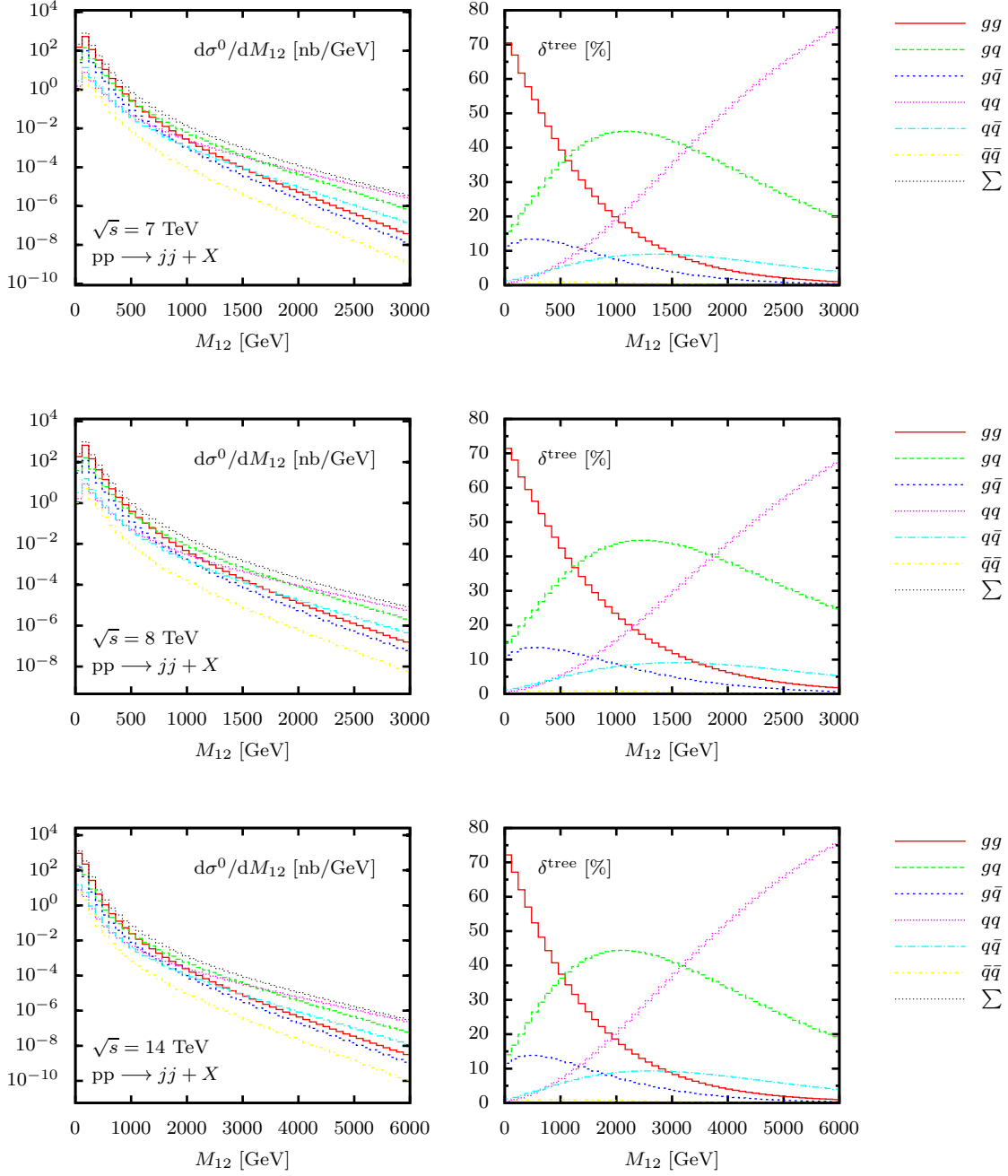


Figure 8: The LO contributions to the dijet invariant mass M_{12} distribution from the different initial-state parton combinations at the LHC with CM energies 7 TeV, 8 TeV, and 14 TeV. Left: absolute predictions; right: relative contributions δ^{tree} .

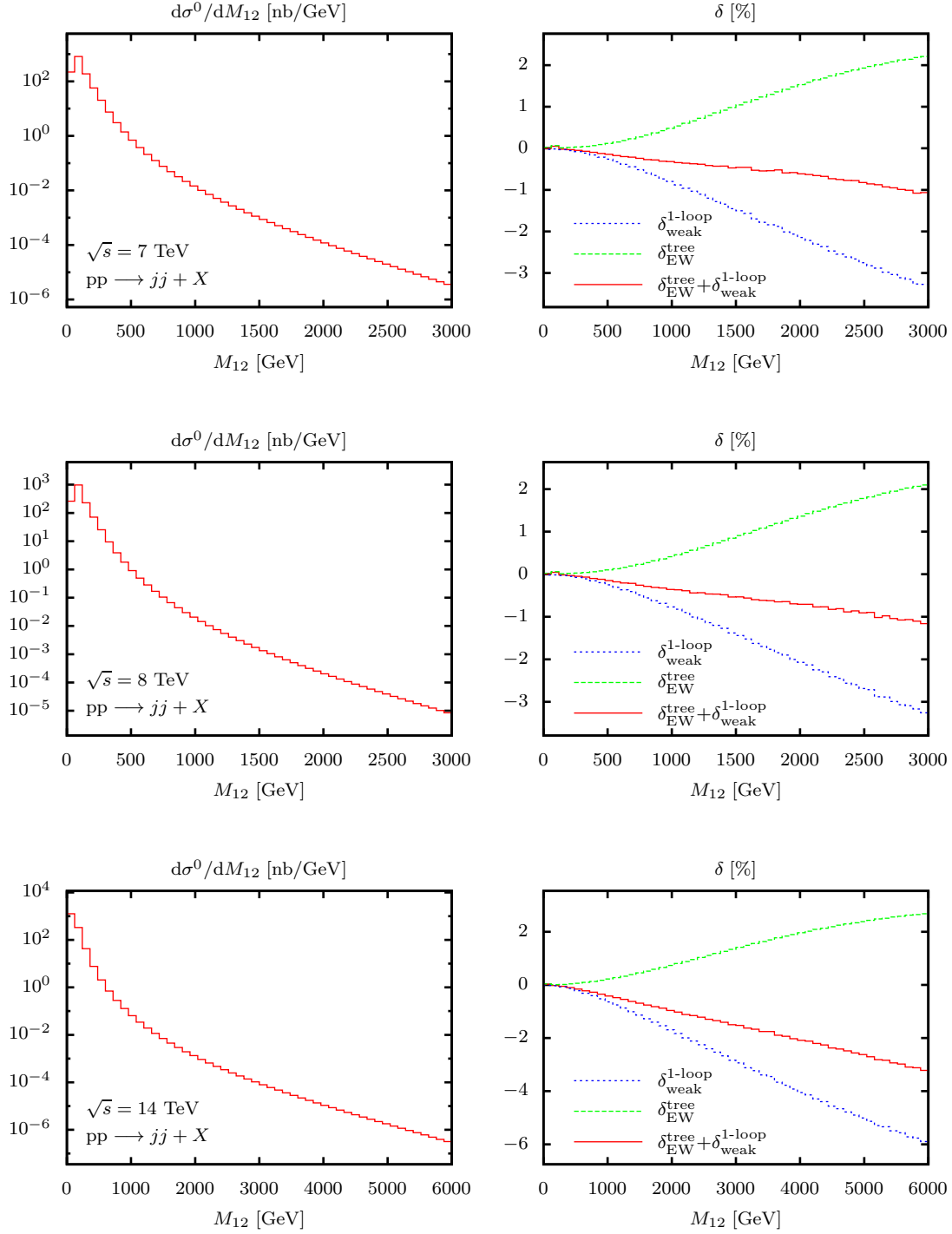


Figure 9: Differential distributions with respect to the dijet invariant mass M_{12} at the LHC with CM energies 7 TeV, 8 TeV, and 14 TeV. Left: absolute predictions; right: relative contributions δ .

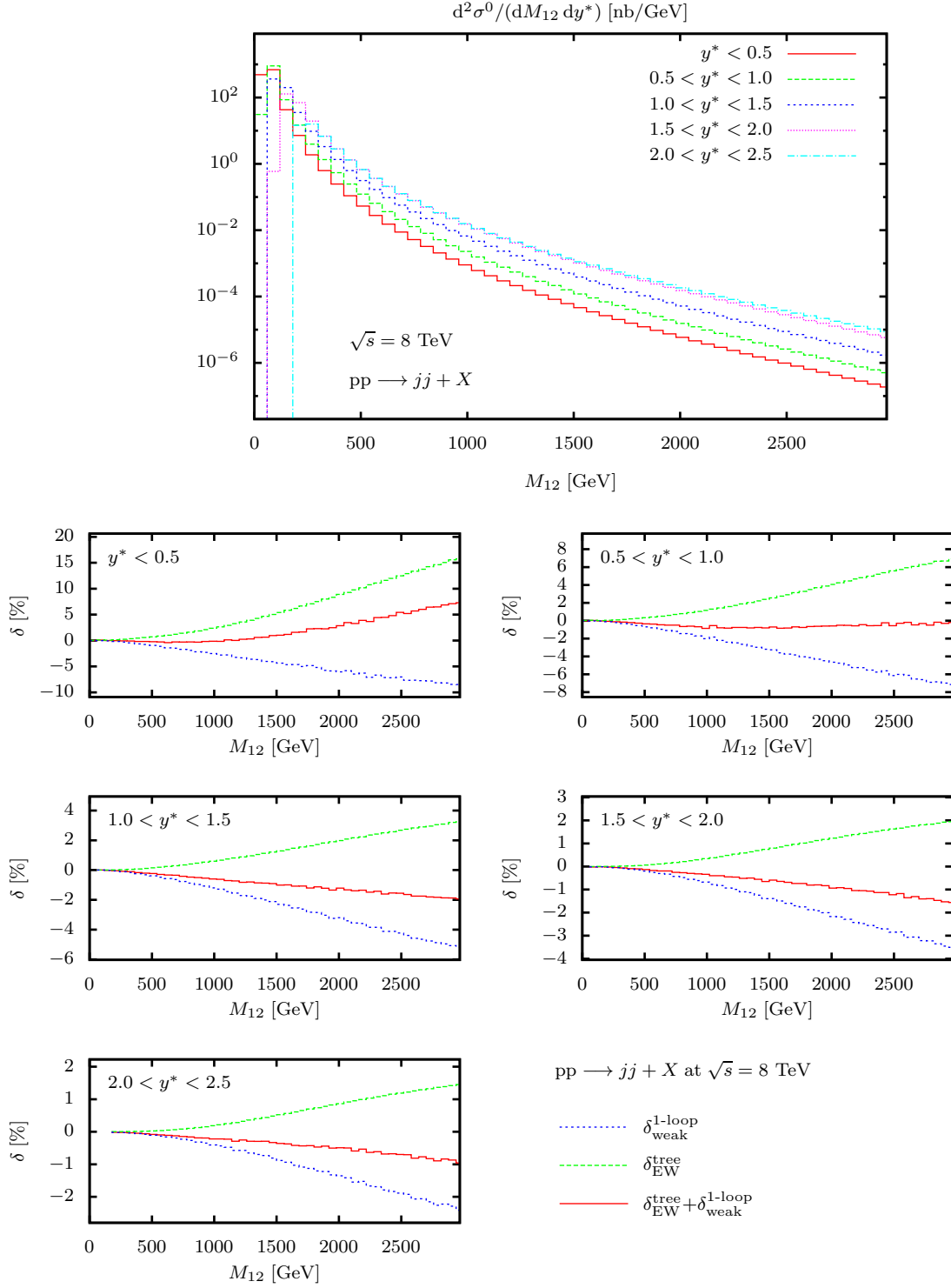


Figure 10: Double-differential distribution with respect to the dijet invariant mass M_{12} and y^* at the LHC with a CM energy of 8 TeV. In the absolute prediction (uppermost plot) the cross section is divided by the bin width in y^* .

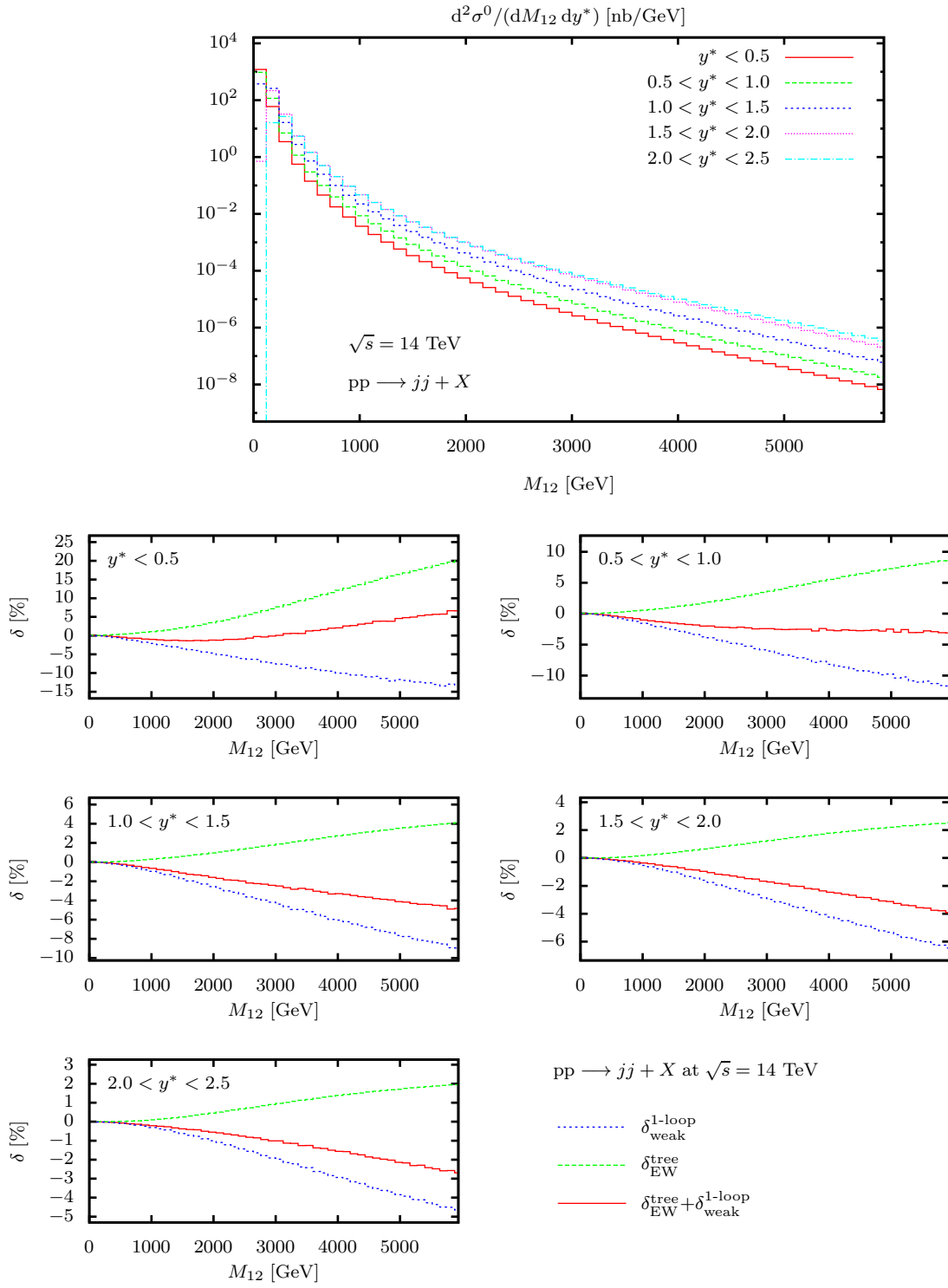


Figure 11: Same as in Fig. 10, but for a CM energy of 14 TeV.

Figures 10 and 11 show the results for the M_{12} distributions corresponding to different rapidity ranges. Specifically, the phase space is divided into different regions of y^* , which is defined as half the rapidity difference of the two leading jets,

$$y^* = \frac{|y_1 - y_2|}{2}. \quad (3.9)$$

For the binning in y^* we have chosen five bins of equal width covering the range $0 < y^* < 2.5$. In all y^* bins we observe the above described behaviour of the relative corrections that increase in magnitude with higher invariant mass, where the tree-level EW contributions and the radiative weak corrections give positive and negative contributions, respectively. Furthermore, a strong dependence on y^* is observed, such that both, $\delta_{\text{EW}}^{\text{tree}}$ and $\delta_{\text{weak}}^{\text{1-loop}}$, are larger for smaller values of y^* . For $\sqrt{s} = 8$ TeV and the invariant mass of 3 TeV the corrections $\delta_{\text{EW}}^{\text{tree}}$ and $\delta_{\text{weak}}^{\text{1-loop}}$ in the first bin ($y^* < 0.5$) amount to approximately 15% and -10% , respectively, whereas in the highest y^* -bin ($2 < y^* < 2.5$) we observe about 1.5% and -2.5% for the respective corrections. As it is evident from the numbers quoted above, $\delta_{\text{EW}}^{\text{tree}}$ decreases more rapidly than $\delta_{\text{weak}}^{\text{1-loop}}$ for higher y^* . The sum of both contributions, thus, has a positive net-contribution for $y^* < 0.5$, gradually decreasing with higher y^* values. In the range of highest y^* ($2 < y^* < 2.5$), even a negative net-contribution results. Qualitatively we observe the same behaviour also at the CM energy of $\sqrt{s} = 14$ TeV. Here we examine dijet invariant masses up to 6 TeV, where we observe approximately 20% and -15% in the first bin ($y^* < 0.5$), and 2% and -5% in the highest y^* -bin ($2 < y^* < 2.5$) for $\delta_{\text{EW}}^{\text{tree}}$ and $\delta_{\text{weak}}^{\text{1-loop}}$, respectively.

As already indicated in the discussion of integrated cross sections above, the behaviour of the corrections can be better understood by identifying the Sudakov regime in phase space. For the contributions with $2 \rightarrow 2$ kinematics, i.e. the LO cross sections and the virtual corrections, the following relations hold:

$$|\hat{y}_1| = |-\hat{y}_2| = y^*, \quad \hat{s} = M_{12}^2, \quad \hat{t} = -\frac{M_{12}^2}{1 + e^{\pm 2y^*}}, \quad \hat{u} = -\frac{M_{12}^2}{1 + e^{\mp 2y^*}}, \quad (3.10)$$

where \hat{y}_i and \hat{s} , \hat{t} , \hat{u} denote the rapidity and the partonic Mandelstam variables. The two different signs refer to $\hat{y}_1 \gtrless 0$. For large $M_{12} \gg M_W$ and small y^* we reside in the Sudakov regime, where all scales are simultaneously large compared to the vector-boson masses. Here, all logarithms of the form $\alpha_w \ln^2(Q^2/M_V^2)$, with $Q^2 = \hat{s}, -\hat{t}, -\hat{u}$ become large, leading to the observed enhancements of the weak radiative corrections. As can be seen in the absolute distributions in Figs. 10 and 11, however, this regime delivers only a small fraction to the cross section if the high-energy region is defined via cuts on the invariant mass M_{12} .

Although the corrections $\delta_{\text{EW}}^{\text{tree}}$ show a similar behaviour, their origin is of a completely different nature: As discussed above, the bulk of the contributions to $\delta_{\text{EW}}^{\text{tree}}$ originate from the qq -initiated processes, in particular from the partonic subprocesses $uu \rightarrow uu$ and $ud \rightarrow ud$. Owing to their colour structure, the interference terms of $\mathcal{O}(\alpha_s \alpha)$ considered here receive contributions from products of t -, u -, and s -channel diagrams only, but not from squares of those topologies. Therefore, these interferences appear to be more central than the larger LO QCD contributions which are dominated by squared topologies.

In summary, for high M_{12} , where the corrections are largest, the cross section is dominated by the contribution coming from the highest possible y^* values. However, this

pp \rightarrow $jj + X$ at $\sqrt{s} = 7$ TeV

$k_{T,1}/\text{GeV}$	25 - ∞	50 - ∞	100 - ∞	200 - ∞	500 - ∞	1000 - ∞	1500 - ∞
σ^0/nb	78600(2)	5417.1(1)	291.205(9)	11.1765(2)	$63.697(2) \cdot 10^{-3}$	$396.843(8) \cdot 10^{-6}$	$5.9746(10) \cdot 10^{-6}$
$\sigma_{\text{QCD}}^0/\text{nb}$	78561(2)	5413.8(2)	290.517(9)	11.0873(3)	$61.251(2) \cdot 10^{-3}$	$353.47(1) \cdot 10^{-6}$	$4.9611(9) \cdot 10^{-6}$
$\delta_{\text{weak}}^{1\text{-loop}}/\%$	-0.02	-0.10	-0.34	-0.99	-2.96	-5.12	-6.13
$\delta_{\text{EW}}^{\text{tree}}/\%$	0.05	0.06	0.24	0.80	3.99	12.28	20.44
$\sum \delta/\%$	0.02	-0.04	-0.10	-0.19	1.04	7.16	14.31
$\sigma^{\text{NLO}}/\text{nb}$	78581(2)	5411.9(1)	290.216(9)	11.0664(3)	$61.887(4) \cdot 10^{-3}$	$378.76(4) \cdot 10^{-6}$	$5.6705(8) \cdot 10^{-6}$

pp \rightarrow $jj + X$ at $\sqrt{s} = 8$ TeV

$k_{T,1}/\text{GeV}$	25 - ∞	50 - ∞	100 - ∞	200 - ∞	500 - ∞	1000 - ∞	1500 - ∞
σ^0/nb	94683(2)	6762.3(2)	380.68(1)	15.7387(5)	$105.965(3) \cdot 10^{-3}$	$877.88(2) \cdot 10^{-6}$	$20.4538(3) \cdot 10^{-6}$
$\sigma_{\text{QCD}}^0/\text{nb}$	94638(2)	6759.0(3)	379.90(1)	15.6330(6)	$102.626(2) \cdot 10^{-3}$	$795.70(3) \cdot 10^{-6}$	$17.3482(2) \cdot 10^{-6}$
$\delta_{\text{weak}}^{1\text{-loop}}/\%$	-0.02	-0.09	-0.33	-0.97	-2.96	-5.35	-6.70
$\delta_{\text{EW}}^{\text{tree}}/\%$	0.04	0.05	0.21	0.68	3.26	10.33	17.90
$\sum \delta/\%$	0.02	-0.04	-0.12	-0.29	0.30	4.98	11.20
$\sigma^{\text{NLO}}/\text{nb}$	94661(2)	6756.1(2)	379.44(1)	15.5871(6)	$102.932(5) \cdot 10^{-3}$	$835.29(9) \cdot 10^{-6}$	$19.292(3) \cdot 10^{-6}$

pp \rightarrow $jj + X$ at $\sqrt{s} = 14$ TeV

$k_{T,1}/\text{GeV}$	25 - ∞	50 - ∞	100 - ∞	200 - ∞	500 - ∞	1000 - ∞	2500 - ∞
σ^0/nb	198483(4)	16194.3(5)	1074.11(3)	56.405(2)	$671.10(2) \cdot 10^{-3}$	$12.0383(4) \cdot 10^{-3}$	$8.8504(2) \cdot 10^{-6}$
$\sigma_{\text{QCD}}^0/\text{nb}$	198410(5)	16189.7(5)	1072.85(4)	56.204(1)	$661.52(2) \cdot 10^{-3}$	$11.5060(2) \cdot 10^{-3}$	$7.4826(2) \cdot 10^{-6}$
$\delta_{\text{weak}}^{1\text{-loop}}/\%$	-0.02	-0.08	-0.28	-0.84	-2.72	-5.48	-10.49
$\delta_{\text{EW}}^{\text{tree}}/\%$	0.03	0.03	0.12	0.36	1.44	4.62	18.28
$\sum \delta/\%$	0.01	-0.05	-0.15	-0.48	-1.28	-0.86	7.79
$\sigma^{\text{NLO}}/\text{nb}$	198443(4)	16181.6(5)	1071.15(3)	55.935(2)	$653.10(3) \cdot 10^{-3}$	$11.4076(10) \cdot 10^{-3}$	$8.066(1) \cdot 10^{-6}$

Table 2: Integrated dijet cross sections and respective corrections for various ranges of the transverse momentum of the leading jet $k_{T,1}$ at the LHC with CM energies 7 TeV, 8 TeV, and 14 TeV.

region receives the smallest corrections, leading to the small corrections that we observe in Table 1 even for very high M_{12} cuts. As we will see in the next section, this behaviour is reversed in case of the transverse-momentum distributions. Despite the different origin of the relative corrections $\delta_{\text{weak}}^{1\text{-loop}}$ and $\delta_{\text{EW}}^{\text{tree}}$, they conspire together to large cancellations in the sum $\delta_{\text{EW}}^{\text{tree}} + \delta_{\text{weak}}^{1\text{-loop}}$. The degree of this compensation, however, depends on the chosen cuts defining the observable.

3.3.2 The transverse momenta of the leading and subleading jet at the LHC

In Table 2 we list the various integrated cross sections at LO, the NLO cross section, and the correction factors defined above for different cuts on the transverse momentum of the leading jet, $k_{T,1}$. The cut $k_{T,1} > 25$ GeV in the first column is already imposed by the

default set of cuts and does not represent a further restriction to the cross section. Again, the integrated cross section decreases rapidly with more restrictive cuts on the transverse momentum, indicating that the cross section, and with it the corrections, are dominated by the region with the lowest accepted $k_{T,1}$.

The weak radiative corrections display the expected Sudakov-type behaviour with increasing negative corrections for higher $k_{T,1}$ -cuts and only a modest dependence on the CM energy of the collider. For cut values of 25 GeV up to 1.5 TeV they increase from -0.02% to -6% for $\sqrt{s} = 7$ TeV. For $\sqrt{s} = 14$ TeV and a cut of $k_{T,1} > 2.5$ TeV the radiative corrections even amount to -11% . The LO EW contributions show a much stronger dependence on the collider energy than the loop corrections, in particular for more restrictive cuts. This \sqrt{s} dependence is also stronger than the one observed for the dijet invariant-mass spectra discussed in the previous section.

Considering that $k_{T,1} \leq M_{12}/2$ at LO and that the cross section as well as the corrections are dominated by the region of lowest accepted M_{12} , one might naively expect that the results for a fixed cut on $k_{T,1}$ should be comparable to the respective corrections for a M_{12} cut of twice that value. However, the region close to $M_{12} \approx 2k_{T,1}$ at LO requires central jet production in the partonic CM frame, i.e. $y^* \approx 0$, so that the cross section defined via the $k_{T,1}$ cut is dominated by the Sudakov regime. This explains the smaller cross section and the larger corrections as compared to the cross section defined via the corresponding M_{12} cut discussed in the previous section.

The differential distributions in $k_{T,1}$ shown in Fig. 12 cover the range up to $k_{T,1} = 1.5$ TeV for $\sqrt{s} = 7$ TeV, 8 TeV, and up to $k_{T,1} = 3$ TeV for $\sqrt{s} = 14$ TeV and further underline the observations made above. The weak corrections display the expected behaviour from the Sudakov logarithms with corrections reaching up to -6% at $k_{T,1} = 1.5$ TeV for $\sqrt{s} = 7$ TeV, 8 TeV, and -12% at $k_{T,1} = 3$ TeV for $\sqrt{s} = 14$ TeV. On the other hand, the tree-level corrections $\delta_{EW}^{\text{tree}}$ increase with higher $k_{T,1}$ and reach approximately 16% at $k_{T,1} = 1.5$ TeV for $\sqrt{s} = 7$ TeV, 8 TeV, and 20% at $k_{T,1} = 3$ TeV for $\sqrt{s} = 14$ TeV, resulting in significant cancellations in the sum $\delta_{EW}^{\text{tree}} + \delta_{\text{weak}}^{1\text{-loop}}$.

By introducing a further binning in y^* we obtain the double differential distributions shown in Figs. 13 and 14. At higher values of the transverse momentum, the production of the jets is required to be more and more central in the partonic CM frame, leading to the observed rapid decrease in the cross section for the bins with higher values of y^* . In contrast to the M_{12} distribution, the bin with the smallest value for y^* is the most dominant in the high- $k_{T,1}$ tail. Moreover, both the tree-level EW corrections $\delta_{EW}^{\text{tree}}$ and the one-loop weak radiative corrections $\delta_{\text{weak}}^{1\text{-loop}}$ are only slightly affected by the y^* binning, while there is a significant dependence in the M_{12} distribution discussed in the previous section.

Additionally, we present the corresponding transverse-momentum distributions with respect to the subleading jet in Figs. 15 and 17. Recall that leading and subleading jets have the same transverse momenta ($k_{T,1} = k_{T,2}$) in all $2 \rightarrow 2$ particle configurations, i.e. that only the real emission corrections to the four-quark channels show a different behaviour here. In particular, $\delta_{EW}^{\text{tree}}$ remains the same when going from the leading to the subleading jet. On the other hand, the weak loop corrections $\delta_{\text{weak}}^{1\text{-loop}}$ turn out to be more pronounced for small y^* . This is due to the fact that subleading jets fill bins with smaller k_T in the spectra which rapidly decrease with higher k_T 's. Since the positive real-emission

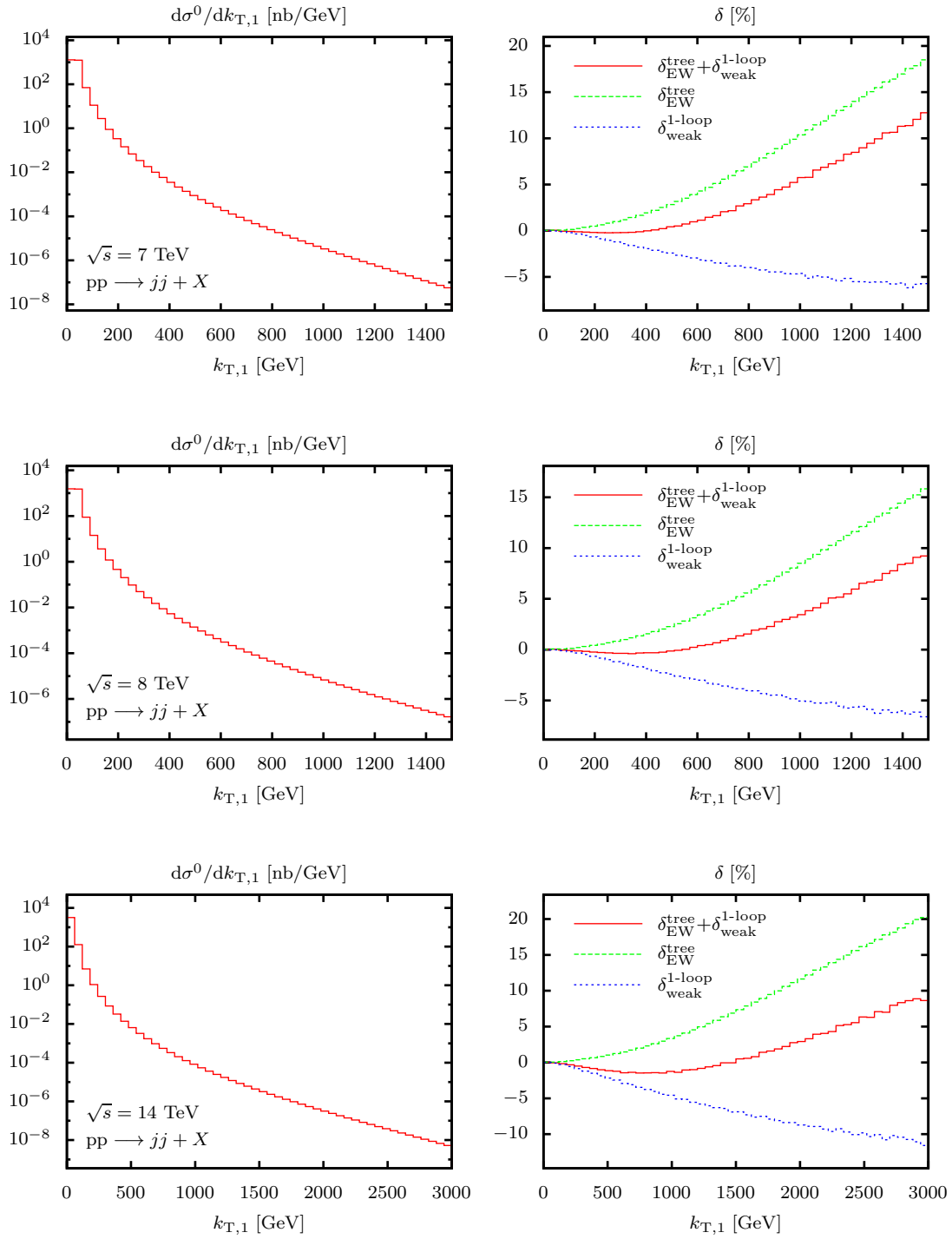


Figure 12: Differential distributions with respect to the transverse momentum of the leading jet $k_{T,1}$ at the LHC with CM energies 7 TeV, 8 TeV, and 14 TeV. Left: absolute predictions; right: relative contributions δ .

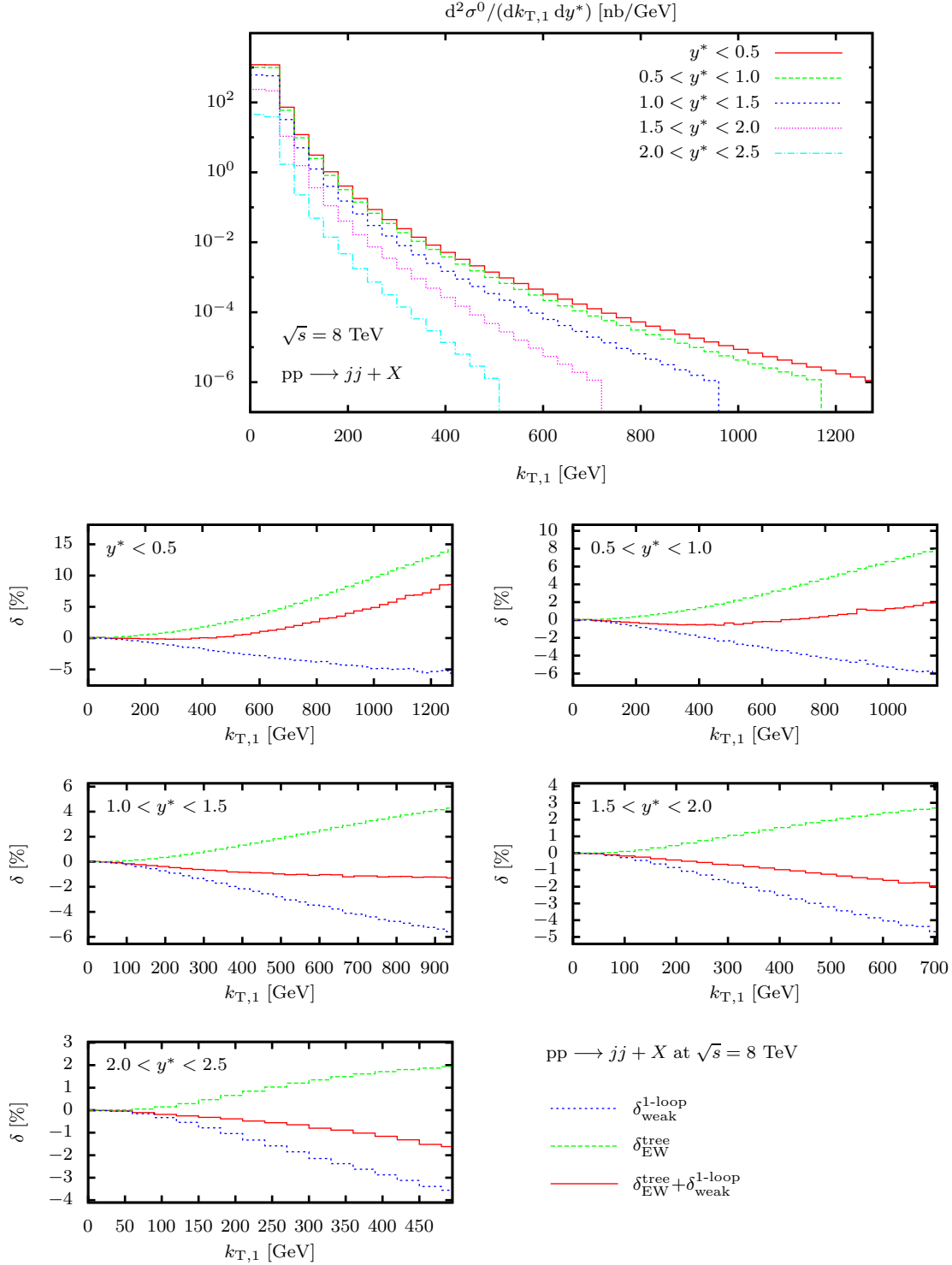


Figure 13: Double-differential distribution with respect to the transverse momentum of the leading jet $k_{T,1}$ and y^* at the LHC with a CM energy of 8 TeV. In the absolute prediction (uppermost plot) the cross section is divided by the bin width in y^* .

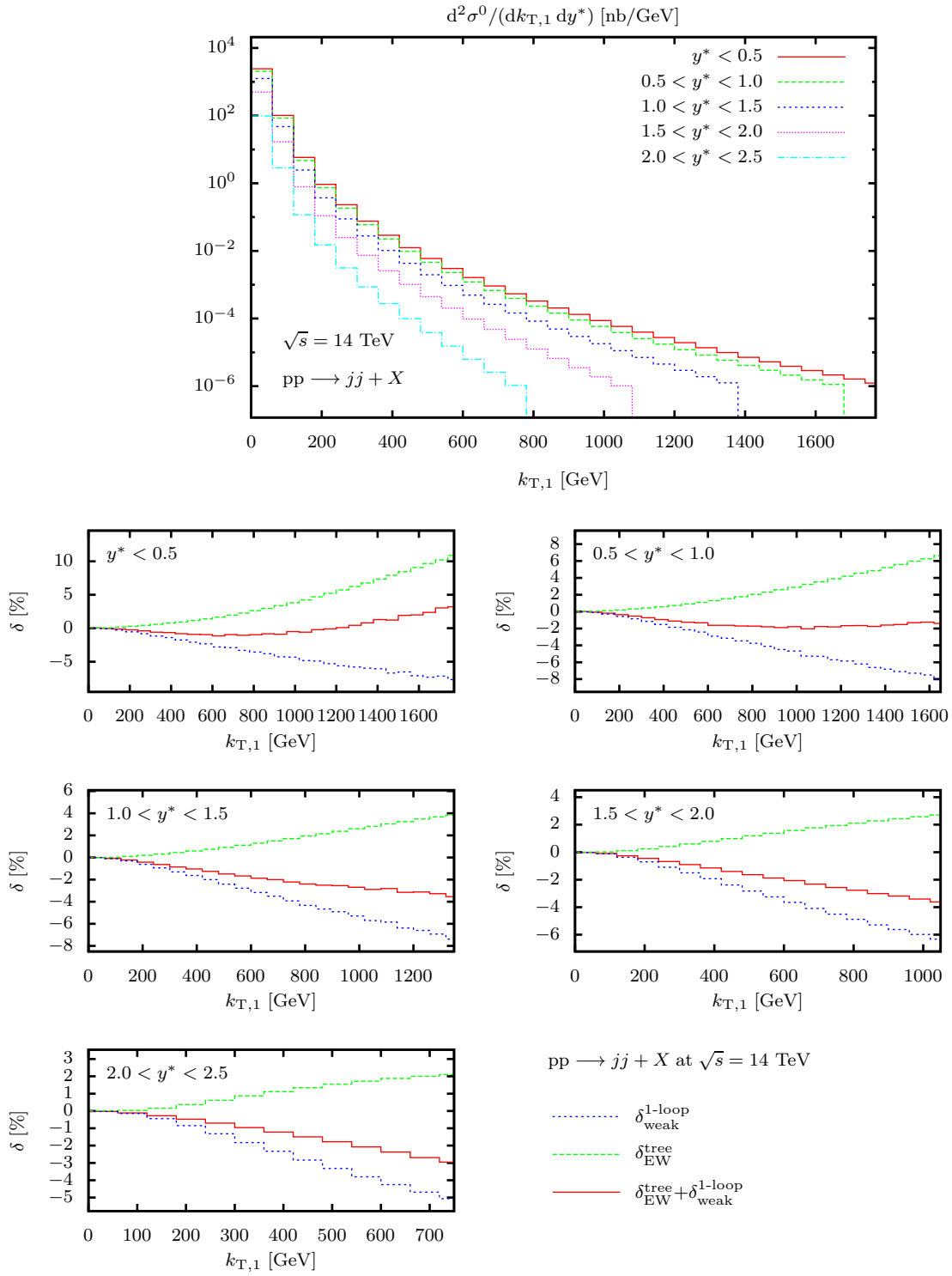


Figure 14: Same as in Fig. 13, but for a CM energy of 14 TeV.

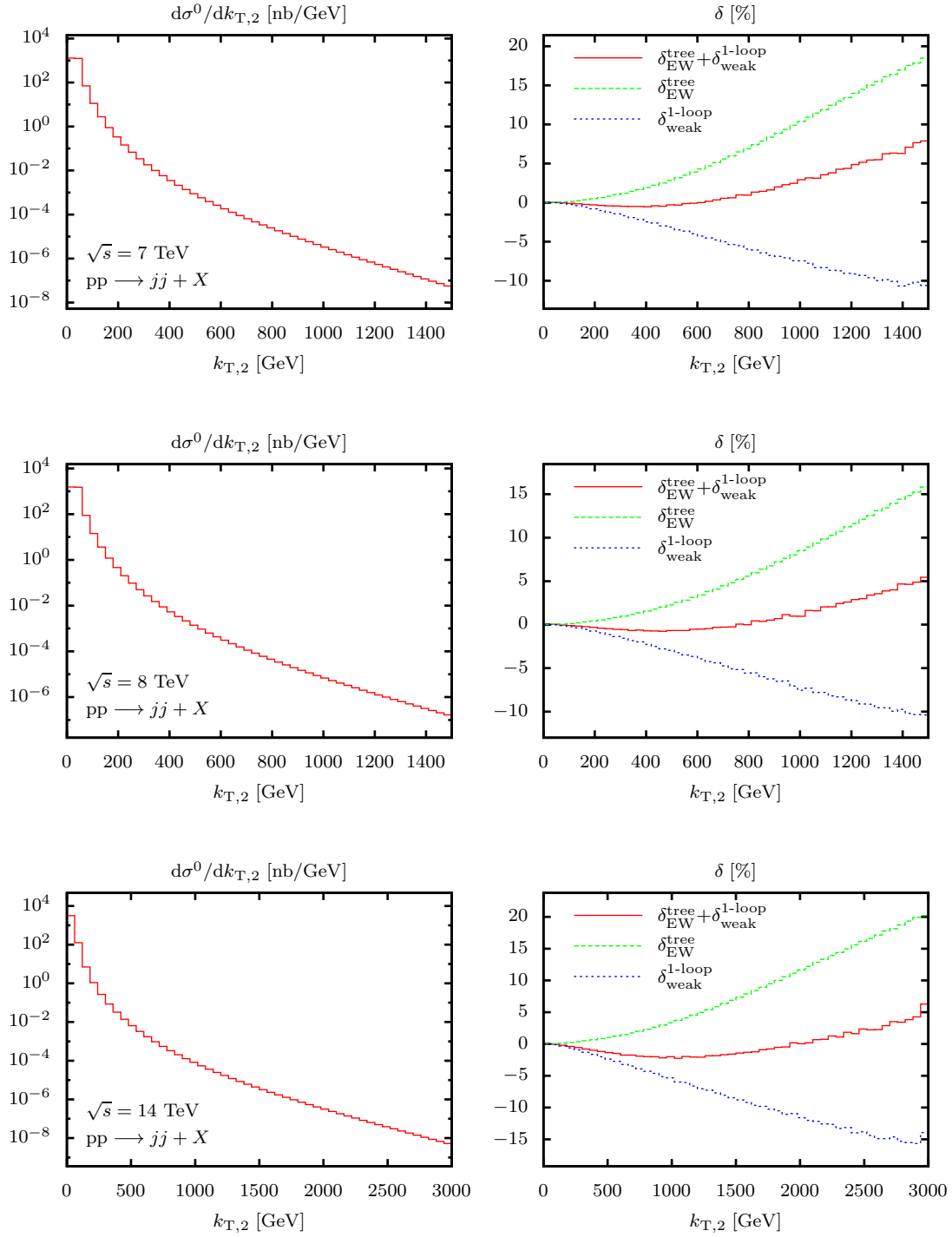


Figure 15: Differential distributions with respect to the transverse momentum of the subleading jet $k_{T,2}$ at the LHC with CM energies 7 TeV, 8 TeV, and 14 TeV. Left: absolute predictions; right: relative contributions δ .

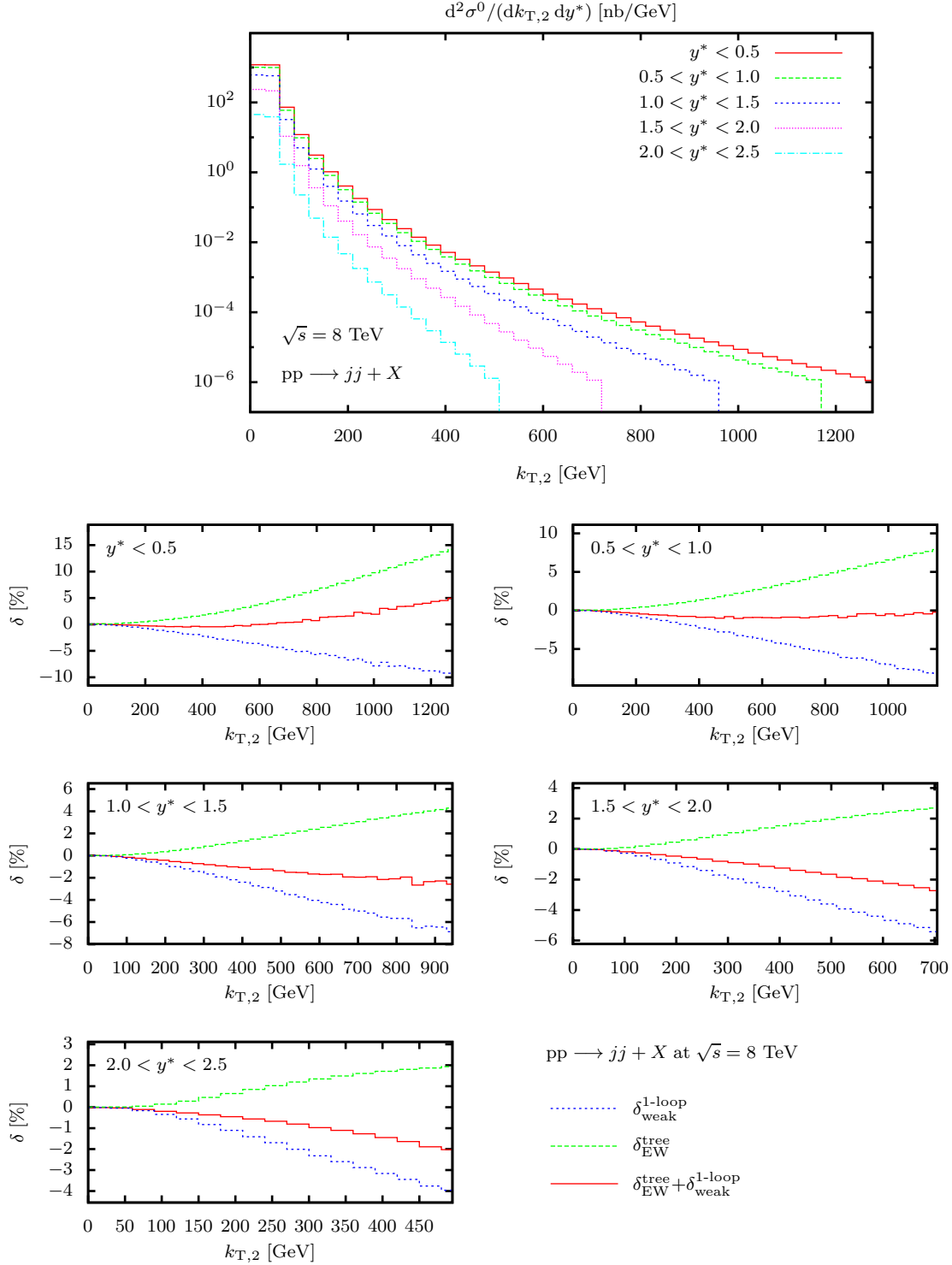


Figure 16: Double-differential distribution with respect to the transverse momentum of the subleading jet $k_{T,2}$ and y^* at the LHC with a CM energy of 8 TeV. In the absolute prediction (uppermost plot) the cross section is divided by the bin width in y^* .

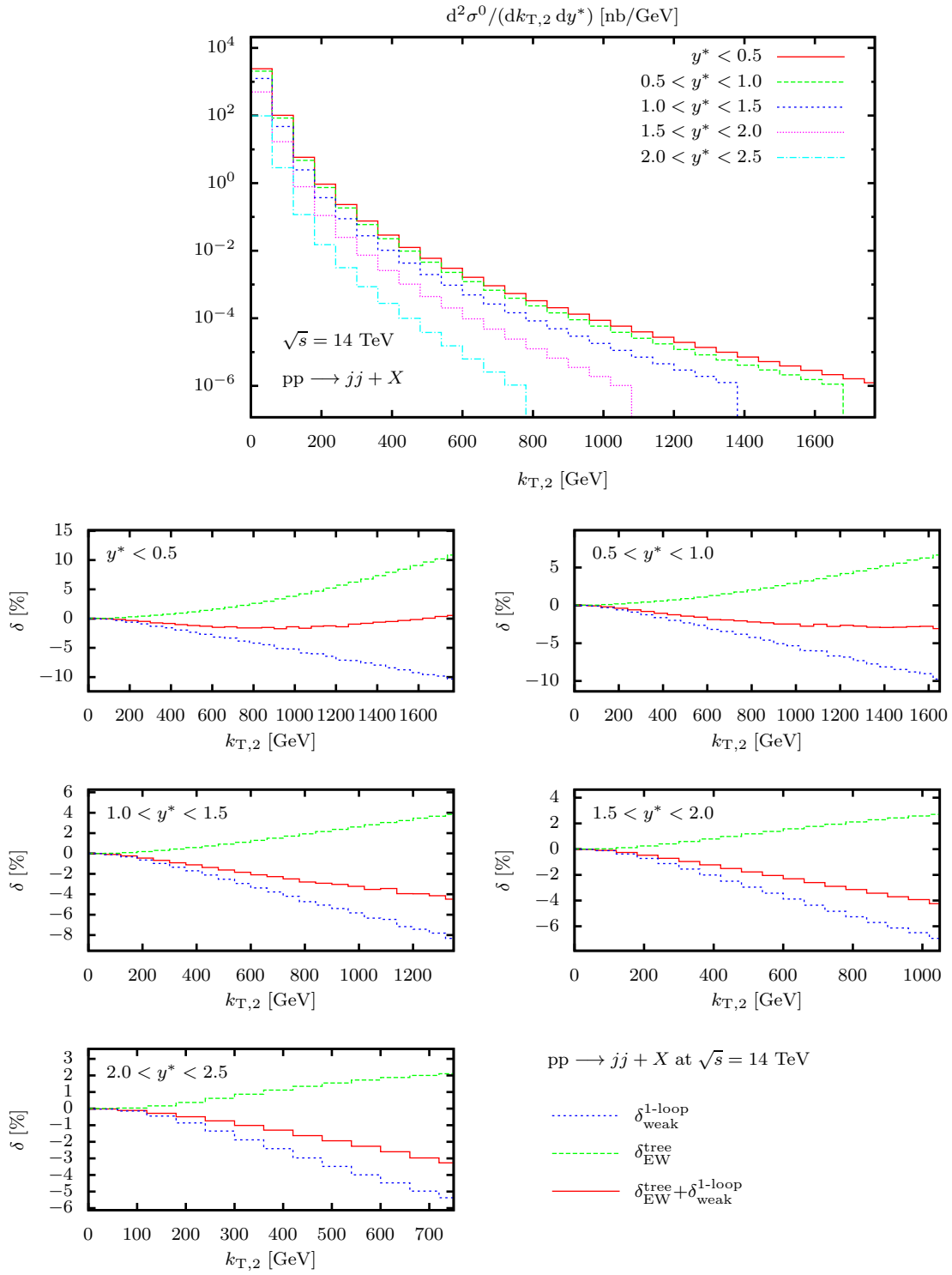


Figure 17: Same as in Fig. 16, but for a CM energy of 14 TeV.

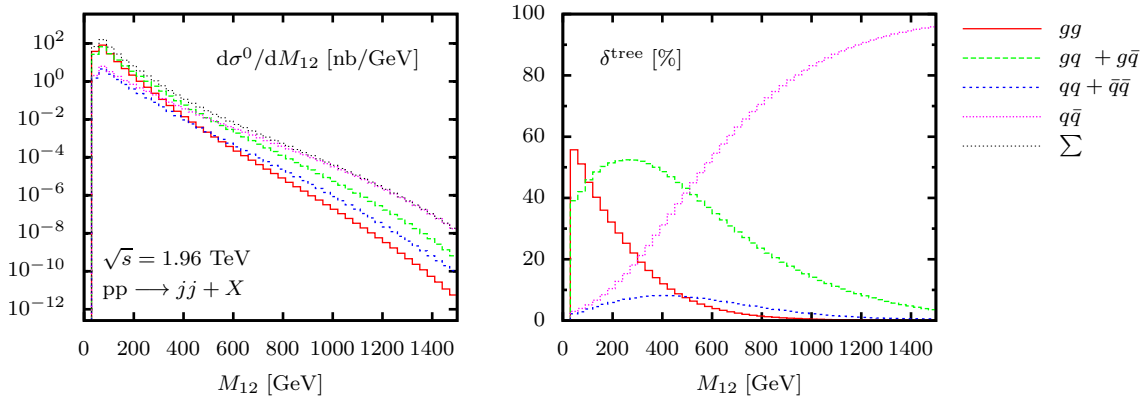


Figure 18: The LO contributions to the dijet invariant mass M_{12} distribution from the different initial-state parton combinations at the Tevatron. Left: absolute predictions; right: relative contributions δ^{tree} .

contribution on the k_T axis of the subleading jets is, thus, shifted to the left as compared to the leading jet, the sum of negative virtual and positive real corrections for a fixed bin is somewhat shifted to more negative values for the subleading jet. This effect is largest for the smallest y^* where the cross section is largest, because the real emission has a particular tendency to reduce maxima in distributions.

3.3.3 Dijet production at the Tevatron

In the following, we present the results for dijet production at the Tevatron, i.e. for a $p\bar{p}$ initial state and a CM energy of $\sqrt{s} = 1.96$ TeV.

Figure 18 shows the various contributions of the different partonic channels at LO contributing to dijet production at the Tevatron for the invariant-mass distribution of the two jets. Since the Tevatron is a $p\bar{p}$ collider, with valence quark–antiquark pairs in the initial state, there is a strong $q\bar{q}$ dominance at large values of the invariant mass M_{12} (several hundred GeV), which requires large scattering energies and thus large momentum fraction x of the partons. At the moderate values $M_{12} \lesssim 500$ GeV, there is still some dominance of channels with gluons in the initial state, with even the largest contribution from gg scattering for very low M_{12} , because the gluon PDF has the strongest rise at small x .

The differential distributions with respect to the dijet invariant mass M_{12} , the transverse momentum of the leading jet $k_{T,1}$ and the subleading jet $k_{T,2}$ are shown in Fig. 19(a–c), respectively. In accordance with the observations made for the LHC, the weak corrections $\delta_{\text{weak}}^{1\text{-loop}}$ are much smaller for M_{12} -based observables as compared to those based on the transverse momenta of the jets. We further observe that the LO EW contributions $\delta_{\text{EW}}^{\text{tree}}$ in the M_{12} distribution is similar in magnitude and opposite in sign as compared to $\delta_{\text{weak}}^{1\text{-loop}}$, similarly to the case of the LHC. For the transverse-momentum distributions, however, $\delta_{\text{EW}}^{\text{tree}}$ becomes negative for higher $k_{T,i}$, further increasing the corrections in $\delta_{\text{EW}}^{\text{tree}} + \delta_{\text{weak}}^{1\text{-loop}}$, which reach around -12% for $k_{T,i} = 800$ GeV. It is interesting to note that the radiative corrections $\delta_{\text{weak}}^{1\text{-loop}}$ are similar for both, the leading and subleading jet k_T , which is different

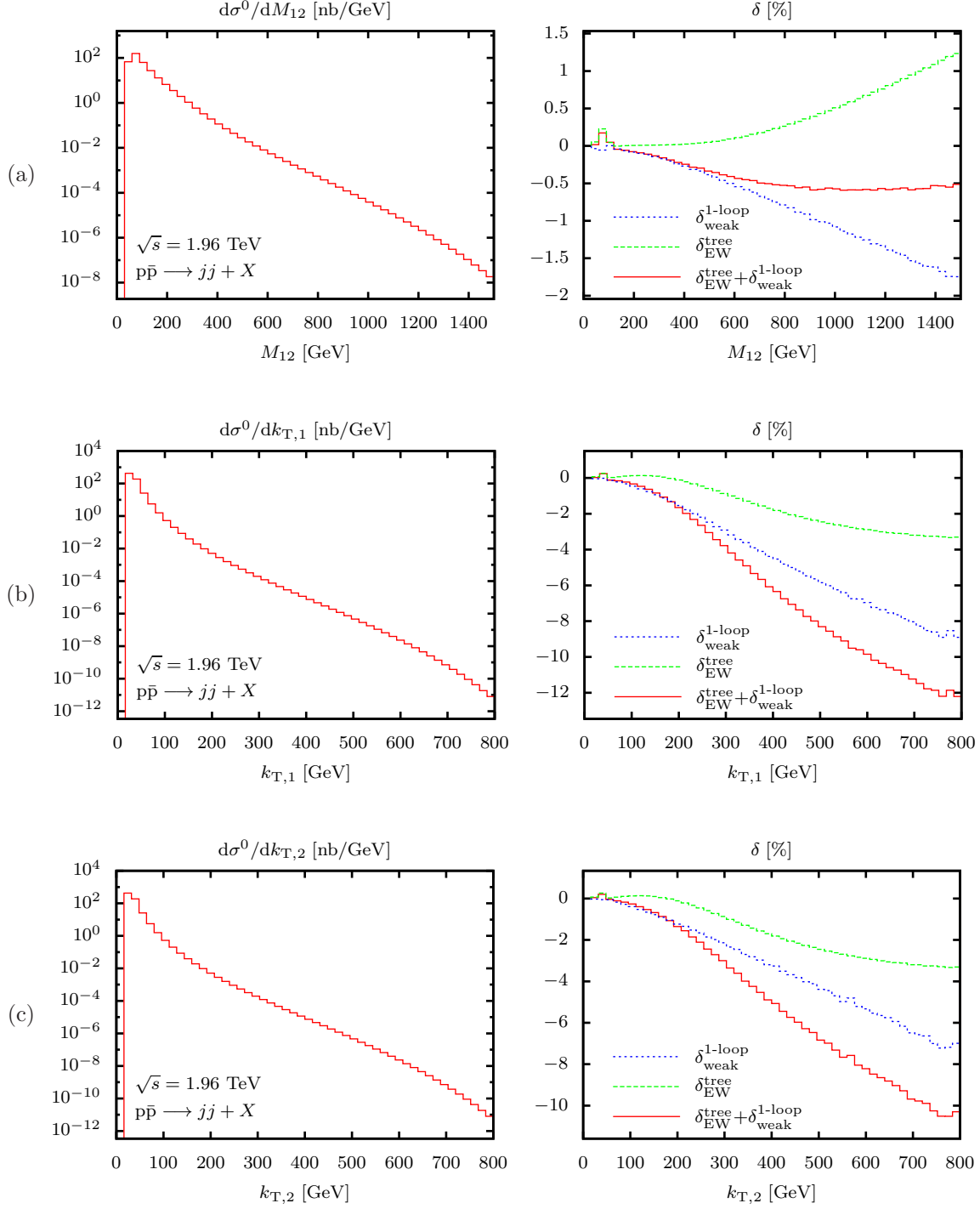


Figure 19: Differential distributions with respect to the dijet invariant mass M_{12} (a), the transverse momentum of the leading jet $k_{T,1}$ (b) and the subleading jet $k_{T,2}$ (c) at the Tevatron for a CM energy of 1.96 TeV. Left: absolute predictions; right: relative contributions δ .

from the behaviour we observed at the LHC, where the corrections to $k_{T,2}$ are significantly larger. To understand this, recall that the difference in the corrections for leading and subleading jets is merely due to real emission corrections in the four-quark channels. These are the real QCD corrections to the interference of weak and QCD tree diagrams. Generically these interferences, which are part of $\delta_{EW}^{\text{tree}}$ in LO, are much smaller at the Tevatron than at the LHC, as is obvious from $\delta_{EW}^{\text{tree}}$ in Fig. 19. Moreover, it is interesting that the corrections are even slightly larger for the leading jet than for the subleading one, because the real QCD corrections to the weak–QCD interference are negative at high energy scales, as also observed for $\delta_{EW}^{\text{tree}}$ before.

The M_{12} and $k_{T,1}$ distributions with a further binning in y^* are shown in Figs. 20 and 21.

3.3.4 Comparison to other work

Preliminary results for the weak radiative corrections to dijet production at the LHC have been presented by A. Scharf in the proceedings contribution [18], where the contributions from external bottom quarks were not considered as part of dijet production, but discussed separately. For comparison, we here adopt the calculational setup of Ref. [18] for the LHC,

$$\begin{aligned}
\sqrt{s} &= 14 \text{ TeV}, & k_{T,1}^{\text{cut}} &= k_{T,2}^{\text{cut}} = 50 \text{ GeV}, \\
y^{\text{cut}} &: \text{none}, & \mu_F = \mu_R &= 2k_T^{\text{cut}} = 100 \text{ GeV}, \\
\alpha_s &= 0.1, & \alpha &= 1/128, \\
M_W &= 80.425 \text{ GeV}, & M_Z &= 91.1876 \text{ GeV}, \\
\text{PDF set} &: \text{CTEQ6L}, & &
\end{aligned} \tag{3.11}$$

which is partially inferred from Ref. [19]. According to the author of Ref. [18], further details on the jet algorithm and the precise treatment of the W/Z resonances are not available anymore, but those loose ends should only play a minor role. This is confirmed in Fig. 22 which shows our result on the corrections to the transverse-momentum spectrum of the leading jet in comparison to the one shown to Fig. 9 of Ref. [18]. The two results show good agreement over the considered $k_{T,1}$ range.

We have also tried to perform a tuned comparison to the results of Ref. [17], but have not found agreement.³

4 Conclusions

In this paper we have presented the calculation of the most important electroweak corrections to dijet production at the LHC and the Tevatron. These corrections comprise electroweak contributions of $\mathcal{O}(\alpha_s\alpha, \alpha^2)$ to the LO QCD prediction as well as NLO corrections through the order $\alpha_s^2\alpha$. Guided by the electroweak Sudakov-type logarithms induced by soft or collinear W/Z exchange at high energies, we have restricted ourselves to the calculation of the purely weak loop corrections in a first step.

³To find the source of discrepancy seems to require a careful comparison of individual components of the calculation. Since the correctness of our results is backed by our two calculations and the comparison to Ref. [18], we do not see a reason to await the outcome of this procedure before publication.

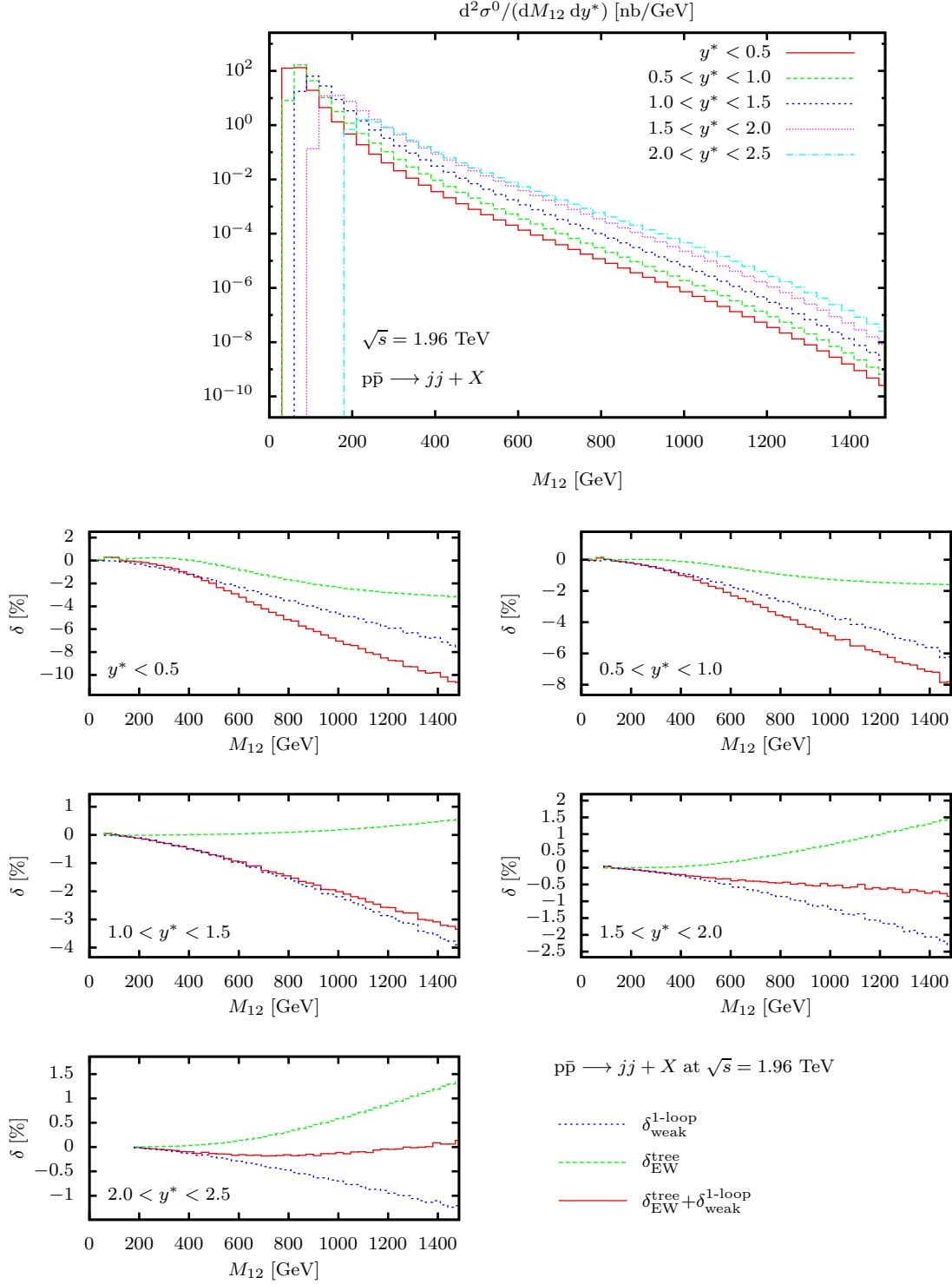


Figure 20: Double-differential distribution with respect to the dijet invariant mass M_{12} and y^* at the Tevatron. In the absolute prediction (uppermost plot) the cross section is divided by the bin width in y^* .

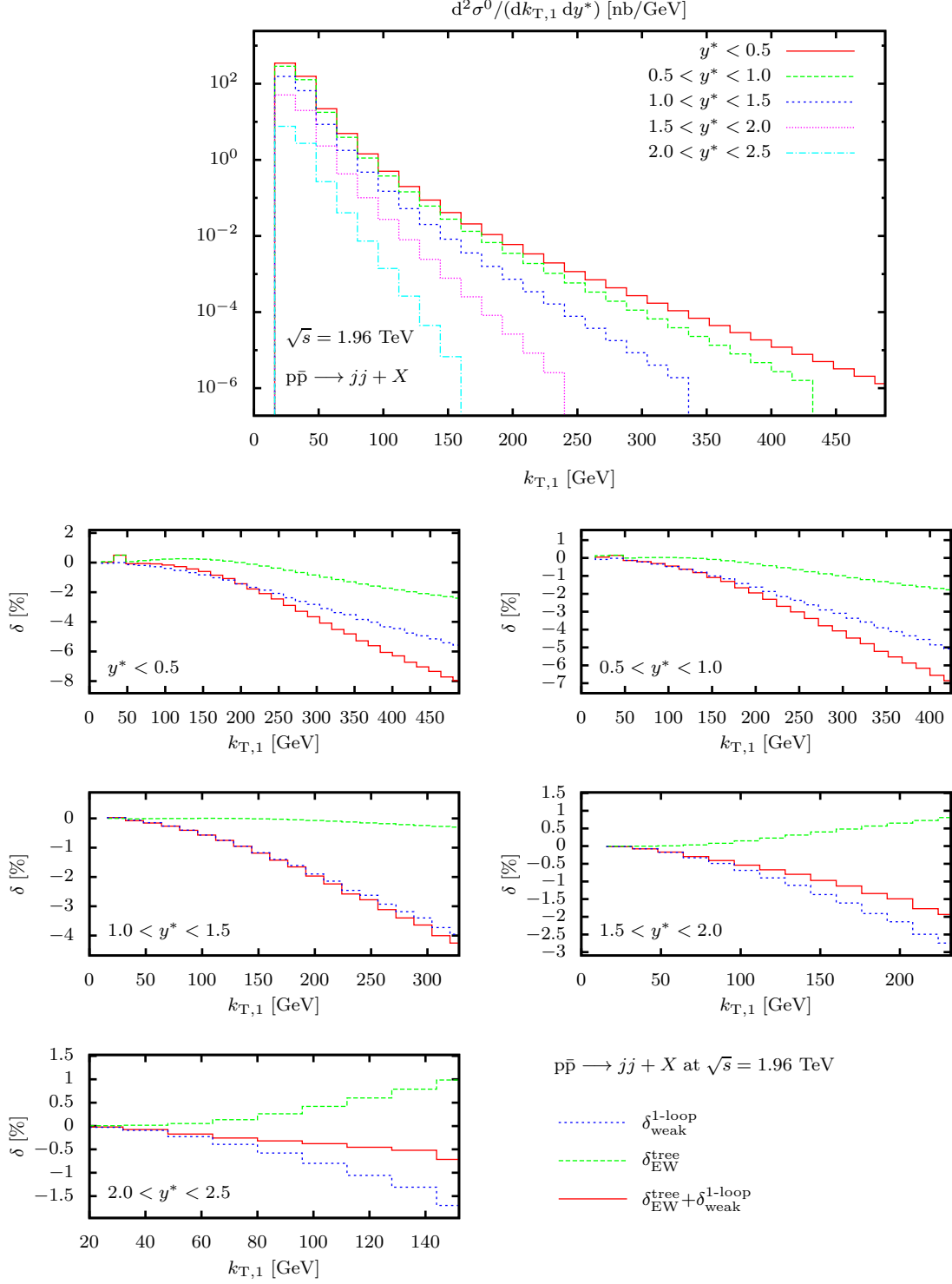


Figure 21: Double-differential distribution with respect to the transverse momentum of the leading jet $k_{T,1}$ and y^* at the Tevatron. In the absolute prediction (uppermost plot) the cross section is divided by the bin width in y^* .

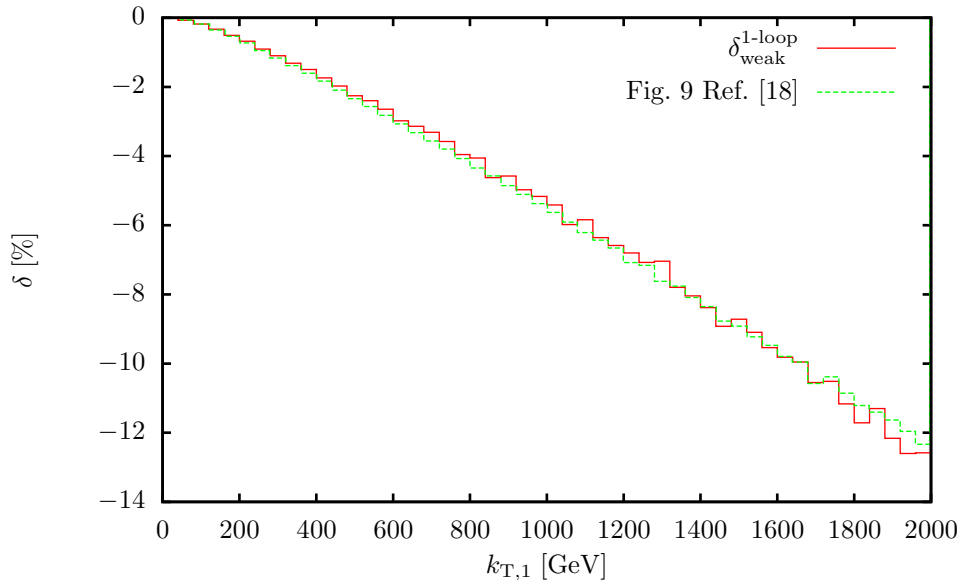


Figure 22: Comparison of the weak one-loop correction $\delta_{\text{weak}}^{\text{1-loop}}$ to the transverse-momentum spectrum of the leading jet as obtained from our calculation to the result of Ref. [18].

For the integrated cross section with minimal cuts we find that the weak corrections are negligible, typically staying below the per-cent level, both at the LHC and the Tevatron. However, the electroweak Sudakov logarithms affect the tails of kinematic distributions that are sensitive to the high energy scales of the hard scattering process. We have discussed this feature in some detail, considering the distributions in the dijet invariant mass (M_{12}), and in the transverse momenta of the leading ($k_{T,1}$) and the subleading ($k_{T,2}$) jets.

For the $\sqrt{s} = 14$ TeV LHC setup, we observe weak loop corrections of $\mathcal{O}(\alpha_s^2\alpha)$ reaching up to -12% (-16%) for a transverse momentum of $k_T = 3$ TeV of the leading (subleading) jet, whereas the dijet invariant-mass distribution only receives weak corrections up to -6% for $M_{12} = 6$ TeV. This difference is explained by the fact that observables based on specific ranges in M_{12} are not dominated by the Sudakov regime (large energies at fixed angles) for large M_{12} values, but rather characterized by the Regge (forward) regime. The weak corrections to dijet production at the Tevatron show similar features, though their size is smaller (-10% for $k_T = 800$ GeV) than for the LHC because of the smaller scattering energy.

The LO EW contributions of $\mathcal{O}(\alpha_s\alpha, \alpha^2)$ turn out to be of the same order of magnitude as the weak loop corrections. At the LHC, these two types of corrections partially cancel, but the degree of this cancellation depends on the chosen observable, setup, and cuts, so that the full calculation is necessary in order to correctly include the considered electroweak effects. At the Tevatron the LO electroweak corrections are somewhat smaller than the weak loop effects, but of the same sign at high transverse jet momenta, thus somewhat enhancing the electroweak effects to -12% at $k_T = 800$ GeV.

The electroweak corrections considered in this paper are supposed to be the by far dominant electroweak effects in dijet production at hadron colliders. Their numerical

impact of 10–20% in the TeV range is not negligible and will certainly play a significant role once the NNLO QCD corrections are known. In contrast to the weak corrections, which get dominated by the large Sudakov logarithms at high energies, the so-far-neglected photonic loop corrections do not receive particular enhancements over their parametric suppression by the electromagnetic coupling α . The calculation of these effects, which are expected to stay at the few-per-cent level, are left to the future.

Acknowledgements

A.H. is supported by the German Research Foundation (DFG) via grant DI 784/2-1.

References

- [1] R. M. Harris and K. Kousouris, *Int. J. Mod. Phys. A* **26** (2011) 5005 [arXiv:1110.5302 [hep-ex]].
- [2] G. Aad *et al.* [ATLAS Collaboration], *Phys. Rev. D* **86** (2012) 014022 [arXiv:1112.6297 [hep-ex]].
- [3] CMS Collaboration, CMS-PAS-QCD-11-004.
- [4] T. Aaltonen *et al.* [CDF Collaboration], *Phys. Rev. D* **78** (2008) 052006 [Erratum-*ibid.* **79** (2009) 119902] [arXiv:0807.2204 [hep-ex]].
- [5] V. M. Abazov *et al.* [D0 Collaboration], *Phys. Rev. D* **85** (2012) 052006 [arXiv:1110.3771 [hep-ex]].
- [6] B. L. Combridge, J. Kripfganz and J. Ranft, *Phys. Lett. B* **70** (1977) 234.
- [7] S. D. Ellis, Z. Kunszt and D. E. Soper, *Phys. Rev. Lett.* **64** (1990) 2121.
- [8] S. D. Ellis, Z. Kunszt and D. E. Soper, *Phys. Rev. Lett.* **69** (1992) 1496.
- [9] W. T. Giele, E. W. N. Glover and D. A. Kosower, *Phys. Rev. Lett.* **73** (1994) 2019 [hep-ph/9403347].
- [10] T. Gehrmann, *PoS DIS 2010* (2010) 004 [arXiv:1007.2107 [hep-ph]].
- [11] A. Gehrmann-De Ridder, *PoS ICHEP 2010* (2010) 106.
- [12] P. Bolzoni, G. Somogyi and Z. Trocsanyi, *JHEP* **1101** (2011) 059 [arXiv:1011.1909 [hep-ph]].
- [13] R. Boughezal, A. Gehrmann-De Ridder and M. Ritzmann, *JHEP* **1102** (2011) 098 [arXiv:1011.6631 [hep-ph]].
- [14] A. Gehrmann-De Ridder, E. W. N. Glover and J. Pires, *JHEP* **1202** (2012) 141 [arXiv:1112.3613 [hep-ph]].
- [15] T. Gehrmann and P. F. Monni, *JHEP* **1112** (2011) 049 [arXiv:1107.4037 [hep-ph]].

- [16] A. G. -D. Ridder, T. Gehrmann and M. Ritzmann, arXiv:1207.5779 [hep-ph].
- [17] S. Moretti, M. R. Nolten and D. A. Ross, Nucl. Phys. B **759** (2006) 50 [hep-ph/0606201].
- [18] A. Scharf, arXiv:0910.0223 [hep-ph].
- [19] J. H. Kühn, A. Scharf and P. Uwer, Phys. Rev. D **82** (2010) 013007 [arXiv:0909.0059 [hep-ph]].
- [20] V. S. Fadin, L. N. Lipatov, A. D. Martin and M. Melles, Phys. Rev. D **61** (2000) 094002 [hep-ph/9910338].
- [21] M. Ciafaloni, P. Ciafaloni and D. Comelli, Phys. Rev. Lett. **84** (2000) 4810 [hep-ph/0001142].
- [22] M. Hori, H. Kawamura and J. Kodaira, Phys. Lett. B **491** (2000) 275 [hep-ph/0007329].
- [23] M. Melles, Eur. Phys. J. C **24** (2002) 193 [hep-ph/0108221].
- [24] W. Beenakker and A. Werthenbach, Nucl. Phys. B **630** (2002) 3 [hep-ph/0112030].
- [25] A. Denner, M. Melles and S. Pozzorini, Nucl. Phys. B **662** (2003) 299 [hep-ph/0301241].
- [26] B. Jantzen, J. H. Kühn, A. A. Penin, V. A. Smirnov, and , Phys. Rev. D **72** (2005) 051301 [Erratum-ibid. D **74** (2006) 019901] [hep-ph/0504111].
- [27] B. Jantzen, J. H. Kühn, A. A. Penin, V. A. Smirnov and , Nucl. Phys. B **731** (2005) 188 [Erratum-ibid. B **752** (2006) 327] [hep-ph/0509157].
- [28] U. Baur, Phys. Rev. D **75** (2007) 013005 [hep-ph/0611241].
- [29] J. H. Kühn, A. A. Penin and V. A. Smirnov, Nucl. Phys. Proc. Suppl. **89** (2000) 94 [hep-ph/0005301].
- [30] J. H. Kühn, A. A. Penin and V. A. Smirnov, Eur. Phys. J. C **17** (2000) 97 [hep-ph/9912503].
- [31] S. Dittmaier and M. Krämer, Phys. Rev. D **65** (2002) 073007 [hep-ph/0109062].
- [32] A. Denner, S. Dittmaier, M. Roth and D. Wackerroth, Nucl. Phys. B **560** (1999) 33 [hep-ph/9904472].
- [33] A. Denner, S. Dittmaier, M. Roth and L. H. Wieders, Nucl. Phys. B **724** (2005) 247 [Erratum-ibid. B **854** (2012) 504] [hep-ph/0505042].
- [34] S. Catani and M. H. Seymour, Nucl. Phys. B **485** (1997) 291 [Erratum-ibid. B **510** (1998) 503] [hep-ph/9605323].

- [35] S. Catani, S. Dittmaier, M. H. Seymour and Z. Trocsanyi, Nucl. Phys. B **627** (2002) 189 [hep-ph/0201036].
- [36] S. Dittmaier, Phys. Rev. D **59** (1998) 016007 [hep-ph/9805445].
- [37] T. Hahn, Comput. Phys. Commun. **140** (2001) 418 [hep-ph/0012260].
- [38] T. Hahn and M. Perez-Victoria, Comput. Phys. Commun. **118** (1999) 153 [hep-ph/9807565].
- [39] A. Denner and S. Dittmaier, Nucl. Phys. B **734** (2006) 62 [hep-ph/0509141].
- [40] A. Denner and S. Dittmaier, Nucl. Phys. B **844** (2011) 199 [arXiv:1005.2076 [hep-ph]].
- [41] G. P. Lepage, CLNS-80/447.
- [42] J. Küblbeck, M. Böhm and A. Denner, Comput. Phys. Commun. **60** (1990) 165.
- [43] M. Moretti, T. Ohl and J. Reuter, hep-ph/0102195.
- [44] T. Ohl, Comput. Phys. Commun. **120** (1999) 13 [hep-ph/9806432].
- [45] G. Bell, J. H. Kühn and J. Rittinger, Eur. Phys. J. C **70** (2010) 659 [arXiv:1004.4117 [hep-ph]].
- [46] A. Bredenstein, A. Denner, S. Dittmaier and S. Pozzorini, JHEP **0808** (2008) 108 [arXiv:0807.1248 [hep-ph]].
- [47] A. Denner, Fortsch. Phys. **41** (1993) 307 [arXiv:0709.1075 [hep-ph]].
- [48] T. Kinoshita, J. Math. Phys. **3** (1962) 650.
- [49] T. D. Lee and M. Nauenberg, Phys. Rev. **133** (1964) B1549.
- [50] C. Amsler *et al.* [Particle Data Group Collaboration], Phys. Lett. B **667** (2008) 1 and 2009 partial update for the 2010 edition.
- [51] D. Y. Bardin, A. Leike, T. Riemann and M. Sachwitz, Phys. Lett. B **206** (1988) 539.
- [52] J. Pumplin, D. R. Stump, J. Huston, H. L. Lai, P. M. Nadolsky and W. K. Tung, JHEP **0207** (2002) 012 [hep-ph/0201195].
- [53] M. Cacciari, G. P. Salam and G. Soyez, JHEP **0804** (2008) 063 [arXiv:0802.1189 [hep-ph]].